

# X-Ray Study of Temperature and Abundance Profiles of the Cluster of Galaxies Abell 1060 with Suzaku

Kosuke SATO,<sup>1</sup> Noriko Y. YAMASAKI,<sup>2</sup> Manabu ISHIDA,<sup>2</sup> Yoshitaka ISHISAKI,<sup>1</sup>  
Takaya OHASHI,<sup>1</sup> Hajime KAWAHARA,<sup>3</sup> Takao KITAGUCHI,<sup>3</sup>  
Madoka KAWAHARADA,<sup>3</sup> Motohide KOKUBUN,<sup>3</sup> Kazuo MAKISHIMA,<sup>3</sup>  
Naomi OTA,<sup>4</sup> Kazuhiro NAKAZAWA,<sup>2</sup> Takayuki TAMURA,<sup>2</sup>  
Kyoko MATSUSHITA,<sup>5</sup> Naomi KAWANO,<sup>6</sup> Yasushi FUKAZAWA,<sup>6</sup>  
and John P. HUGHES<sup>7</sup>

<sup>1</sup> *Department of Physics, Tokyo Metropolitan University, 1-1 Minami-Osawa, Hachioji, Tokyo 192-0397*  
*ksato@phys.metro-u.ac.jp*

<sup>2</sup> *Institute of Space and Astronautical Science (ISAS), Japan Aerospace Exploration Agency,*  
*3-1-1 Yoshinodai, Sagami-hara, Kanagawa 229-8510*

<sup>3</sup> *Department of Physics, University of Tokyo, 7-3-1 Hongo, Bunkyo, Tokyo 113-0033*

<sup>4</sup> *Cosmic Radiation Laboratory, The Institute of Physical and Chemical Research (RIKEN),*  
*2-1 Hirosawa, Wako, Saitama 351-0198*

<sup>5</sup> *Department of Physics, Tokyo University of Science, 1-3 Kagurazaka, Shinjuku-ku, Tokyo 162-8601*

<sup>6</sup> *Department of Physical Science, School of Science, Hiroshima University,*  
*1-3-1 Kagamiyama, Higashi-Hiroshima, Hiroshima 739-8526*

<sup>7</sup> *Department of Physics and Astronomy, Rutgers University, Piscataway, NJ 08854-8019, USA*

(Received —; accepted —)

## Abstract

We carried out observations of the central and 20' east offset regions of the cluster of galaxies Abell 1060 with Suzaku. Spatially resolved X-ray spectral analysis has revealed temperature and abundance profiles of Abell 1060 out to 27'  $\simeq$  380  $h_{70}^{-1}$  kpc, which corresponded to  $\sim 0.25 r_{180}$ . Temperature decrease of the intra cluster medium from 3.4 keV at the center to 2.2 keV in the outskirts region are clearly observed. Abundances of Si, S and Fe also decrease by more than 50% from the center to the outer, while Mg shows fairly constant abundance distribution at  $\sim 0.7$  solar within  $r \lesssim 17'$ . O shows lower abundance of  $\sim 0.3$  solar in the central region ( $r \lesssim 6'$ ), and indicates a similar feature with Mg, however it is sensitive to the estimated contribution of the Galactic components of  $kT_1 \sim 0.15$  keV and  $kT_2 \sim 0.7$  keV in the outer annuli ( $r \gtrsim 13'$ ). Systematic effects due to the point spread function tails, contamination on the XIS filters, instrumental background, cosmic and/or Galactic X-ray background, and the assumed solar abundance tables are carefully examined. Results on temperature and abundances of Si, S, and Fe are consistent with those derived by XMM-Newton at  $r \lesssim 13'$ . Formation and metal enrichment process of the cluster are discussed based on the present results.

**Key words:** galaxies: clusters: individual (Abell 1060) — X-rays: galaxies — X-rays: ISM

## 1. Introduction

Clusters of galaxies, being the largest virialized system in the universe, are filled with the intracluster medium (ICM), which consists of X-ray emitting hot plasma with typical temperatures of a few times  $10^7$  K. X-ray spectroscopy of the ICM can immediately determine its temperature and metal abundances. The metal abundances of ICM have a lot of information to understand the chemical history and evolution of clusters. A large amount of metals of the ICM are mainly produced by supernovae (SN) in early-type galaxies (Arnaud et al. 1992; Renzini et al. 1993), which are classified roughly as Type Ia (SN Ia) and Type II (SN II). Si, S and Fe are synthesized in both SN Ia and SN II, while  $\alpha$  elements such as O, Ne, and Mg are mainly in SN II, which are explosions of massive stars

with initial mass above  $\sim 10 M_{\odot}$ . The metals produced in the galaxies are transferred into the ICM by galactic wind and/or ram pressure stripping.

ASCA firstly revealed the distribution of Si and Fe in the ICM (Fukazawa et al. 1998; Fukazawa et al. 2000; Finoguenov et al. 2000; Finoguenov et al. 2001). The derived iron-mass-to-light ratios (IMLR; Ciotti et al. 1991; Renzini et al. 1993; Renzini 1997) are nearly constant in rich clusters and decrease toward poorer systems (Makishima et al. 2001). Recent observations with Chandra and XMM-Newton allowed detailed studies of the metals in the ICM. These observations, however, showed abundance profiles of O, Mg, Si and Fe only for the central regions of very bright clusters or groups of galaxies dominated by cD galaxies in a reliable manner (Finoguenov et al. 2002; Fukazawa et al. 2004; Matsushita

et al. 2003; Tamura et al. 2003). The abundance profiles of O and Mg, in particular for the cluster outer regions, are still poorly determined, because these satellites are characterized by relatively high intrinsic background levels. Tamura et al. (2004) derived IMLR for five clusters within  $250 h_{100}^{-1}$  kpc to be  $\sim 0.01 M_{\odot}/L_{\odot}$ , and the oxygen mass within  $50 h_{100}^{-1}$  kpc for several clusters. However, oxygen-mass-to-light ratios (OMLR) for rich clusters are not reliable due to the lower emissivity of OVII and OVIII lines in higher temperatures. De Grandi & Molendi (2001); Hayakawa et al. (2006) found that clusters associated with cD galaxies and central cool components showed abundance concentration in the cluster center, while clusters without cD galaxies showed flatter profiles. The central metallicity enhancement in the cool core clusters were further studied and the excess metals were shown to be supplied from the cD galaxies (De Grandi et al. 2004).

Abell 1060 (hereafter A 1060) is a nearby cluster of galaxies ( $z = 0.0114$ ) characterized by a smooth and symmetric distribution of intracluster medium (ICM), and has no cD-galaxy at the center. Chandra observation detected very compact X-ray emissions from the central two elliptical galaxies (Yamasaki et al. 2002), and the temperature and abundance distributions were shown to be somewhat inhomogeneous at the cluster center (Hayakawa et al. 2004). Hayakawa et al. (2006) detected a temperature drop by  $\sim 30\%$  from the central region to  $r \sim 13'$  with XMM-Newton, while it had previously been considered as flat on the basis of the ASCA and ROSAT observations (Tamura et al. 1996, Furusho et al. 2001).

This paper reports results from Suzaku observations of A 1060. Owing to the low-background nature of the Suzaku XIS, we are able to measure the temperature and abundance profiles to a much outer region than the previous XMM-Newton study. We use  $H_0 = 70 \text{ km s}^{-1} \text{ Mpc}^{-1}$ ,  $\Omega_{\Lambda} = 1 - \Omega_M = 0.73$  in this paper. At a redshift of  $z = 0.0114$ ,  $1'$  corresponds to  $14 \text{ kpc}$ , and the virial radius,  $r_{180} = 1.95 h_{100}^{-1} \sqrt{k\langle T \rangle} / 10 \text{ keV Mpc}$  (Markevitch et al. 1998), is  $1.53 \text{ Mpc}$  for the average temperature of  $\langle T \rangle = 3 \text{ keV}$  (Hayakawa et al. 2006). Throughout this paper we adopt the Galactic hydrogen column density of  $N_{\text{H}} = 4.9 \times 10^{20} \text{ cm}^{-2}$  (Dickey & Lockman 1990) in the direction of A 1060. Otherwise noted, the solar abundance table is given by Anders & Grevesse (1989), and errors are 90% confidence region for a single interesting parameter.

## 2. Suzaku Observation and Data Reduction

### 2.1. Observation

Suzaku carried out two pointing observations for A 1060 in November 2005, the central region and  $20'$  east offset region, with exposure of 40.5 and 55.5 ks, respectively. The observation log is summarized in table 1, and the combined X-ray Imaging Spectrometers (XIS; Koyama et al. 2006) image in the 0.5–7 keV range is shown in figure 1. We utilize only the XIS data in this paper. The XIS is an X-ray CCD camera, which consists of one back-illuminated sensor (BI = XIS1) and three front-

**Table 2.** Estimated column density of the contaminant for each sensor at the center of CCD in unit of  $10^{18} \text{ cm}^{-2}$ .

	XIS0	XIS1	XIS2	XIS3
Carbon .....	1.37	1.83	2.52	4.04
Oxygen .....	0.228	0.305	0.420	0.673

illuminated sensors (FI = XIS0, XIS2, XIS3). The BI and FI sensors have different advantages. The former has higher quantum efficiency in the soft energy band ( $E \lesssim 1 \text{ keV}$ ), while the latter shows lower instrumental non X-ray background (NXB). The XIS was operated in the Normal clocking mode (no window nor burst option, so 8 s exposure per frame), with the standard  $5 \times 5$  or  $3 \times 3$  editing mode (Koyama et al. 2006).

The optical blocking filters (OBF) of the XIS have been gradually contaminated in time by out-gas from the satellite, and the degradation of the low energy transmission was already significant in November 2005. The thickness of the contaminant is different among sensors, and is also dependent on the location on the CCD. The estimated column density (C/O=6 in number ratio is assumed) at the center of the CCD is listed in table 2, and the calculated X-ray transmission for BI (XIS1) at each annular region is plotted in figure 2.<sup>1</sup> Though the thickness of the OBF contaminant is different on each annulus, this effect is considered in the calculation of the Ancillary Response File (ARF) by the “xissimarngen” Ftools task (Ishisaki et al. 2007). The energy resolution was also degraded slightly (FWHM  $\sim 150 \text{ eV}$  at 5.9 keV) after the launch, due to the radiation damage of the CCD.

### 2.2. Data Reduction

We used the version 0.7 processing data (Mitsuda et al. 2007), and the analysis was performed with HEASoft version 6.0.6 and XSPEC 11.3.2t. We started the event screening from the cleaned event file, in which selection of the event grade and bad CCD column, disposal of non-observational intervals (during maneuver, data-rate low, South Atlantic Anomaly, Earth occultation, bright Earth rim to avoid scattered solar X-ray), and removal of hot and flickering pixels by the “cleansis” Ftools, were already conducted. The exposure time given in table 1 is for the cleaned event file. We further applied the Good-Time Intervals (GTI) given for excluding the telemetry saturation by the XIS team. The light curve of each sensor in the 0.3–10 keV range with 16 s time bin was also examined to reject periods of anomalous event rate greater or less than  $\pm 3\sigma$  around the mean. After the above screenings, remaining exposure of the central observation was 40.2 ks and that of the offset observation was 52.9 or 54.6 ks (FI or BI). These exposures are not so different from those in table 1, which represent that the NXB was almost stable during the both observations. The event screening with the cut-off rigidity (COR) was not performed in our data.

<sup>1</sup> The calibration database file of `ae_xiN_contami_20060525.fits` was used for the estimation of the XIS contamination ( $N = 0, 1, 2, 3$  corresponding to the XIS sensor).

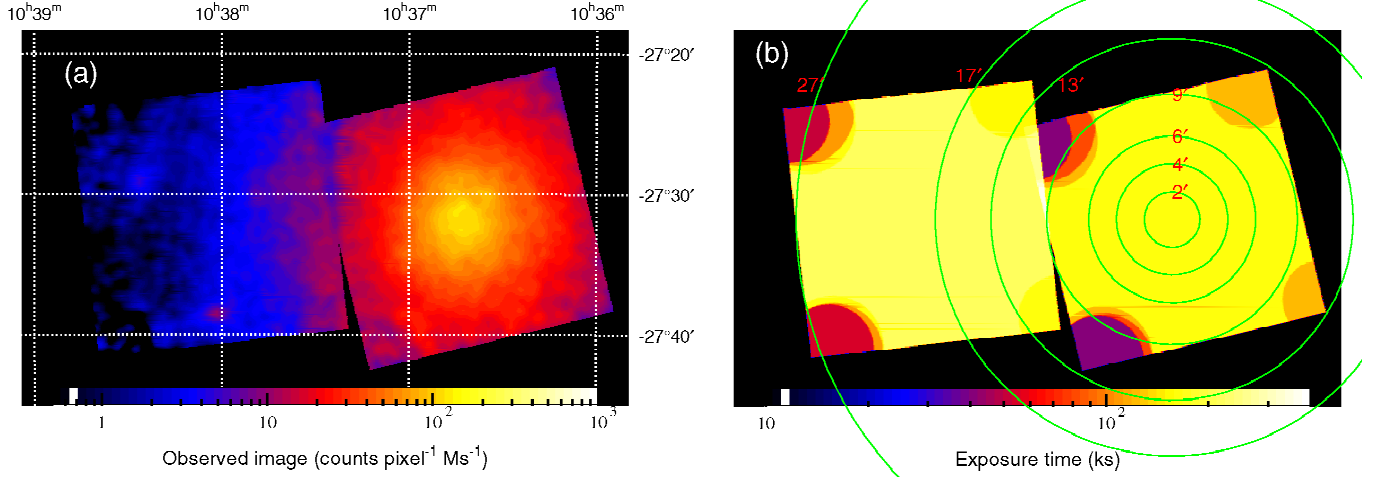


**Fig. 1.** (a) Combined XIS image of the central and offset observations in the 0.5–7.0 keV energy range. The observed XIS0-3 images are added on the sky coordinate after removing each calibration source region, and smoothed with  $\sigma = 16$  pixel  $\simeq 17''$  Gaussian. Estimated components of extragalactic X-ray background (CXB) and instrumental background (NXB) are subtracted, and exposure and vignetting are corrected. (b) Exposure map in ks, in which coordinates of the image are the same with (a). Four XIS sensors are treated separately. Small exposure at the CCD corners correspond to the  $^{55}\text{Fe}$  calibration source locations. The annular regions utilized in the spectral analysis are indicated by green circles.

**Table 1.** Suzaku observation of A 1060 and NGC 2992

Target name	Sequence number	Date	Exposure time	(RA, Dec) in J2000 *	( <i>l</i> , <i>b</i> )
A 1060 center	800003010	2005-Nov-22	40.5 ks	(10 <sup>h</sup> 36 <sup>m</sup> 42 <sup>s</sup> .8, −27°31′42″)	(269°60, 26°49)
A 1060 offset	800004010	2005-Nov-20	55.5 ks	(10 <sup>h</sup> 38 <sup>m</sup> 03 <sup>s</sup> .8, −27°31′42″)	(269°88, 26°65)
NGC 2992 †	700005010	2005-Nov-06	38.8 ks	(09 <sup>h</sup> 45 <sup>m</sup> 45 <sup>s</sup> .2, −14°16′10″)	(249°69, 28°83)
NGC 2992 †	700005020	2005-Nov-19	38.7 ks	(09 <sup>h</sup> 45 <sup>m</sup> 41 <sup>s</sup> .7, −14°16′05″)	(249°66, 28°82)
NGC 2992 †	700005030	2005-Dec-13	48.3 ks	(09 <sup>h</sup> 45 <sup>m</sup> 51 <sup>s</sup> .0, −14°16′51″)	(249°70, 28°84)

\* Average pointing direction of the XIS, written in the RA\_NOM and DEC\_NOM keywords of the event FITS files.

† We used NGC 2992 data to estimate the Galactic component in subsection 4.5.

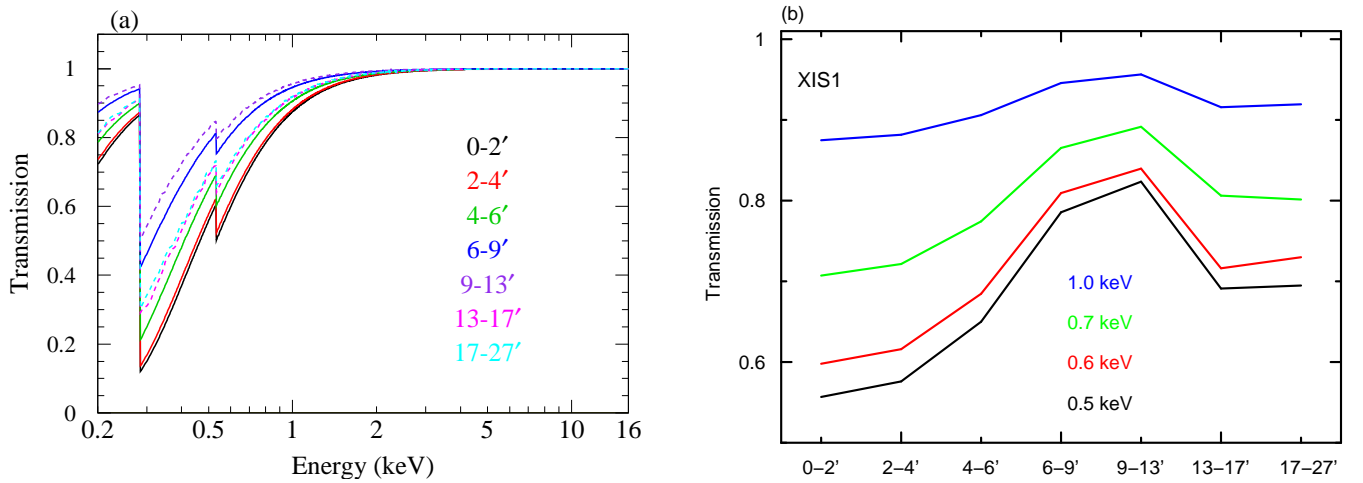


**Fig. 2.** (a) Estimated transmission of the contaminant on the BI (XIS1) sensor for each annular region used in the spectral analysis plotted against the X-ray energy. Transmissions in the central observations are drawn by solid lines, and the offset observations are by dashed lines. These transmissions are calculated by “xissimarfgen” with a calibration file of `ae.xi1.contami.20060525.fits`, and written in the CONTAMI\_TRANSMIS column of the ARF response. (b) The calculated transmission plotted against each annular region in the energies of 0.5, 0.6, 0.7, and 1.0 keV.

### 2.3. NXB & CXB Subtraction

In order to subtract the NXB and the extra-galactic cosmic X-ray background (CXB; see Brandt & Hasinger 2005 for review), we used the night earth database of 770 ks exposure provided by the XIS team for the NXB, and estimated the CXB component using the ASCA results.

The night-earth spectra were extracted from the same detector region as the A 1060 observation in order to cancel positional variation of the NXB. Furthermore, we divided the night-earth data referring to COR in the ranges of  $< 4$  GV, 4–13 GV in 1 GV step, and  $> 13$  GV, because it is known that the intensity and energy spectrum of the NXB are primarily correlated with COR at the orbital location of the satellite. The NXB spectra to be subtracted in the spectral fitting were estimated by adding these COR-sorted night-earth spectra weighted with exposure times of the A 1060 observation in the corresponding COR range.

The CXB component was estimated by the “fake” command of XSPEC using uniform-sky ARFs, which is generated by “xissimarfgen” assuming that the whole sky (practically,  $r < 20'$ ) has the constant intensity and the same X-ray spectrum. We assumed a power-law spectrum for the CXB with the values by Kushino et al. (2002),  $\Gamma = 1.4$  and  $S_X = 5.97 \times 10^{-8}$  erg cm $^{-2}$  s $^{-1}$  sr $^{-1}$  (2–10 keV), absorbed with the neutral hydrogen column of  $N_H = 4.9 \times 10^{20}$  cm $^{-2}$  (Dickey & Lockman 1990). The above CXB intensity is taken from table 3 of Kushino et al. (2002), for the integrated spectrum with source elimination brighter than  $S_0 = 2 \times 10^{-13}$  erg cm $^{-2}$  s $^{-1}$  (2–10 keV) in the GIS filed of view with  $\Gamma = 1.4$  (fix) and the nominal NXB level (0%). It is confirmed that this gives a reasonable estimate of the CXB contribution for the XIS in subsection 6.2 of Ishisaki et al. (2007) and Fujimoto et al. (2007)

Figures 3 (a)–(c) show the background level for Suzaku BI, FI sensors, and XMM-Newton MOS1, at the same 6–9' annulus of the cluster. The observed spectrum after the CXB and NXB subtraction are compared with the estimated CXB and NXB spectra separately for Suzaku, while sum of the CXB and NXB are indicated for the XMM-Newton because the blank-sky data was used as the background. These figures show the background level of Suzaku XIS is  $\sim 50\%$  lower than that of XMM-Newton. It is also notable that there is a strong Al-K $_{\alpha}$  peak at 1.49 keV for the XMM-Newton background, which makes the determination of the Mg abundance quite difficult. The S/N ratio of the Suzaku XIS BI/FI sensors are by about 1.8/2.0 times higher than that of the XMM-Newton MOS at 1 keV, and 1.3/1.8 times higher at 4 keV. The particle background is more stable for Suzaku than XMM-Newton due to its low-earth orbit.

### 3. XMM-Newton Observation & Analysis

The XMM-Newton observation of A 1060 was carried out on 2004 June 29 with total exposure of 64 ks. The same dataset with Hayakawa et al. (2006) was utilized. We used only the MOS data, and data reduction and analy-

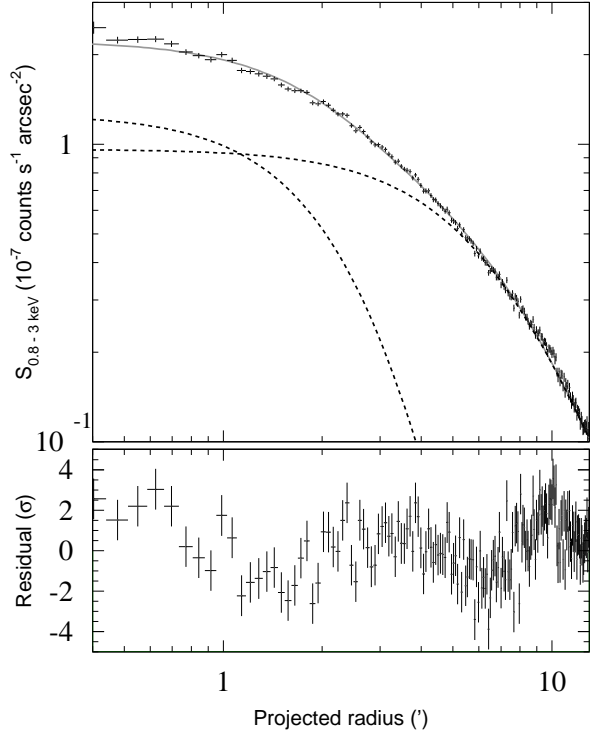


**Fig. 4.** In the upper panel, a radial profile of the surface brightness of A 1060 in the 0.8–3 keV band are plotted for XMM-Newton MOS1+2 ( $r < 13'$ ). The best-fit double- $\beta$  model is shown by the solid gray line, and the two  $\beta$ -components are indicated by dashed lines. In the bottom panel, fit residuals are shown in unit of  $\sigma$ .

**Table 3.** The best-fit parameters of figure 4.

	$\beta$	$r_c$	$S_{0.8-3 \text{ keV}}^*$
narrower . . . .	$1.3 \pm 0.1$	$3.7' \pm 0.3'$	$1.26 \pm 0.14$
wider $\dagger$ . . . . .	0.69 (fix)	7.3' (fix)	$0.96 \pm 0.05$

\*  $S_{0.8-3 \text{ keV}}$  at the center in unit of  $10^{-7}$  counts s $^{-1}$  arcsec $^{-2}$ .

$\dagger$   $\beta$  and  $r_c$  is fixed to the values by Hayakawa et al. (2006).

sis were performed with SAS version 6.0 and HEASoft version 6.0.6. As for the XMM-Newton data, data reduction and spectral analysis were based on Sato et al. (2005) and Hayakawa et al. (2006). Hayakawa et al. (2006) have reported the temperature and abundance profiles with XMM-Newton observation, however, we reanalyzed the data in order to compare with the Suzaku results on the same criterion. The differences from Hayakawa et al. (2006) are: (1) the event extraction region, (2) using the *vapex* thin thermal plasma model (Smith et al. 2001) instead of *vmekal* (Mewe et al. 1985; Mewe et al. 1986), and (3) deriving the element abundances separately.

Utilizing the XMM-Newton image, we also derived the surface brightness profile of A 1060 needed to generate the Suzaku ARFs, because the spatial resolution of XMM-Newton is superior to that of Suzaku. Figure 4 shows a radial profile of A 1060 in the 0.8–3 keV energy range,

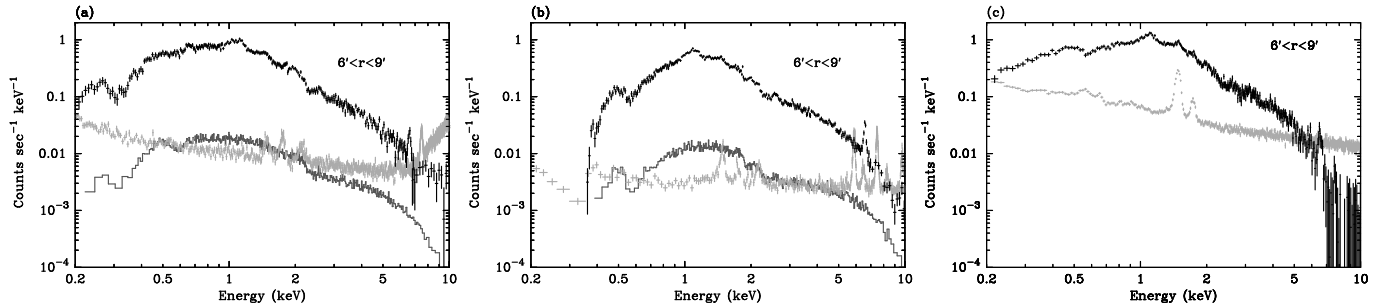


**Fig. 3.** (a) The observed spectrum at the annular region of 6–9′ with the Suzaku BI (XIS1) sensor is plotted in black crosses after subtracting the estimated CXB and NXB components, which are plotted by gray crosses and a black histogram, respectively. (b) Same as (a) but for the FI (XIS0+XIS2+XIS3) sensors. The count rate drop below  $\lesssim 0.4$  keV is due to the event threshold of the FI CCDs (Koyama et al. 2006). Although 0.2–10 keV energy range is shown here, only 0.4–7.1 keV band was utilized for the spectral fitting for both BI and FI. (c) Same as (a) but for the XMM-Newton MOS1 sensor, and the estimated CXB+NXB component using blank-sky observations are plotted in gray. The 0.5–8.0 keV energy range was used for the spectral fitting with XMM-Newton.

fitted with a double- $\beta$  model. The origin of the radial profile is placed at (RA, Dec) = ( $10^{\text{h}}36^{\text{m}}43^{\text{s}}.1$ ,  $-27^{\circ}31'46''$ ) in J2000. The best-fit parameters are summarized in table 3, in which  $\beta$  and  $r_c$  of the wider  $\beta$ -component are fixed to the values by Hayakawa et al. (2006).

## 4. Spectral Analysis and Results

### 4.1. Suzaku XIS Spectra

We extracted spectra from seven annular regions of 0–2′, 2–4′, 4–6′, 6–9′, 9–13′, 13–17′ and 17–27′, centered on (RA, Dec) = ( $10^{\text{h}}36^{\text{m}}42^{\text{s}}.8$ ,  $-27^{\circ}31'42''$ ). The first four annuli were taken from the central observation, and the rest of the three annuli were from the offset observation. Table 4 lists areas of the extraction regions ( $\text{arcmin}^2$ ), coverage of the whole annulus (%), the SOURCE\_RATIO\_REG values (%; see caption for its definition) and the observed counts in 0.4–7.1 keV including NXB and CXB for the BI and FI sensors.

Although the thickness of the OBF contamination is different among sensors as shown in table 2 and figure 5(b), we have confirmed that the four sensors give quite consistent fit results after incorporating the contamination effect into the ARFs, as demonstrated in figure 5(a). We therefore add the three FI spectra (XIS0, XIS2, XIS3), hereafter.

Each annular spectrum is shown in figure 6. The ionized Mg, Si, S, Fe lines are clearly seen in each ring. The O VII and O VIII lines are prominent in the outer rings, however, most of the O VII emission is supposed to come from the local Galactic emission, which will be examined in detail in subsections 4.3–4.5.

### 4.2. Strategy of Spectral Fit

The basic strategy of the spectral fit is described in subsection 6.3 of Ishisaki et al. (2007). The observed spectrum is assumed to contain (A) thin thermal plasma emission from the ICM, (B) local Galactic emission, (C) CXB, and (D) NXB. The estimation of (C) and (D) is described in subsection 2.3, and both are subtracted from the observed spectrum. The spectrum of (B) can be represented by one or two thin-thermal plasma model(s), *apec*, with

**Table 4.** Area, coverage of whole annulus, SOURCE\_RATIO\_REG and observed counts for each annular region. SOURCE\_RATIO\_REG represents the flux ratio in the assumed spatial distribution on the sky (double- $\beta$  model) inside the accumulation region to the entire model, and written in the header keyword of the calculated ARF response by “xissimarfgen”.

Region*	Area <sup>†</sup> ( $\text{arcmin}^2$ )	Coverage <sup>†</sup>	SOURCE_RATIO_REG <sup>‡</sup>		Counts <sup>§</sup>
			RATIO_REG	BI FI	
0–2′	12.6	100.0%	7.7%	30,549	64,606
2–4′	37.7	100.0%	13.7%	55,186	114,220
4–6′	62.8	100.0%	13.8%	49,259	100,080
6–9′	137.0	96.9%	17.2%	52,719	100,750
9–13′	49.1	17.8%	2.8%	10,696	17,329
13–17′	76.2	20.2%	2.2%	11,032	21,010
17–27′	167.3	12.1%	2.0%	18,055	28,834

\* The first four annuli are extracted from the central observation, and others are from the offset observation.

† The largest values among four sensors are presented.

‡ SOURCE\_RATIO\_REG  $\equiv$  Coverage  $\int_{r_{\text{in}}}^{r_{\text{out}}} S(r)r dr / \int_0^{r_{\text{max}}} S(r)r dr$ , where  $S(r)$  represents the radial profile shown in figure 4 and table 3, and the  $r_{\text{max}}$  is set to 30′.

§ Observed counts including NXB and CXB in 0.4–7.1 keV.

1 solar abundance, however, it may vary from field to field by more than an order of magnitude (Kushino et al. 2002). The ICM spectrum (A) can be represented by a variable abundance thin-thermal plasma model, *vapec*, whose best-fit parameters are what we want. An important point is that the spatial distributions are different between (A) and (B). The former follows the surface brightness of the cluster, while the latter is supposed to have almost a uniform distribution in the XIS field of view.

We therefore generated two different ARFs for the spectrum of each annulus,  $A^{\text{U}}$  and  $A^{\text{B}}$ , which respectively assume the uniform-sky emission and  $\sim 1^{\circ} \times 1^{\circ}$  size of the double- $\beta$  surface brightness profile obtained with the XMM-Newton data (table 3).  $A^{\text{U}}$  was used to evaluate the CXB, and the surface brightness of the Galactic component (B) at each annulus in combination with the XSPEC “fakeit” command, and  $A^{\text{B}}$  was used for the actual fitting.

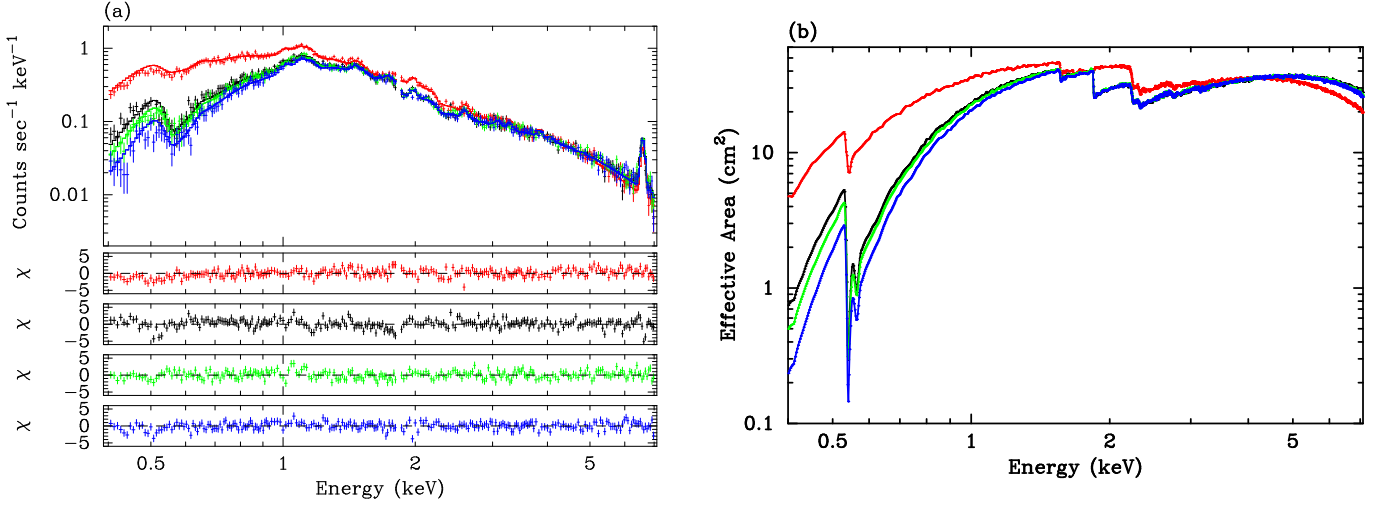


**Fig. 5.** (a) The uppermost panel show the observed spectra after subtracting the estimated CXB and NXB components at the annular region of 2–4′ plotted separately for the XIS0 (black), XIS1 (red), XIS2 (green), and XIS3 (blue) sensors. The cross markers denote the observed spectra and the solid lines show the best-fit model with  $apec_1 + apec_2 + phabs \times vapec$ . The energy range around the Si K-edge (1.825–1.840 keV) is ignored for the spectral fit. Lower three panels show the residuals of the fit in unit of  $\sigma$  for XIS1, XIS0, XIS2, and XIS3 from upper to lower, respectively. (b) Plots of the calculated XIS effective area (ARF + RMF) including the XIS quantum efficiency. These responses are used in the spectral fit in (a) with the same colors. The quantum efficiency is much higher for BI (XIS1; red) than FI sensors, while the OBF contamination is thicker in the order of XIS3, XIS2, XIS1, and XIS0.

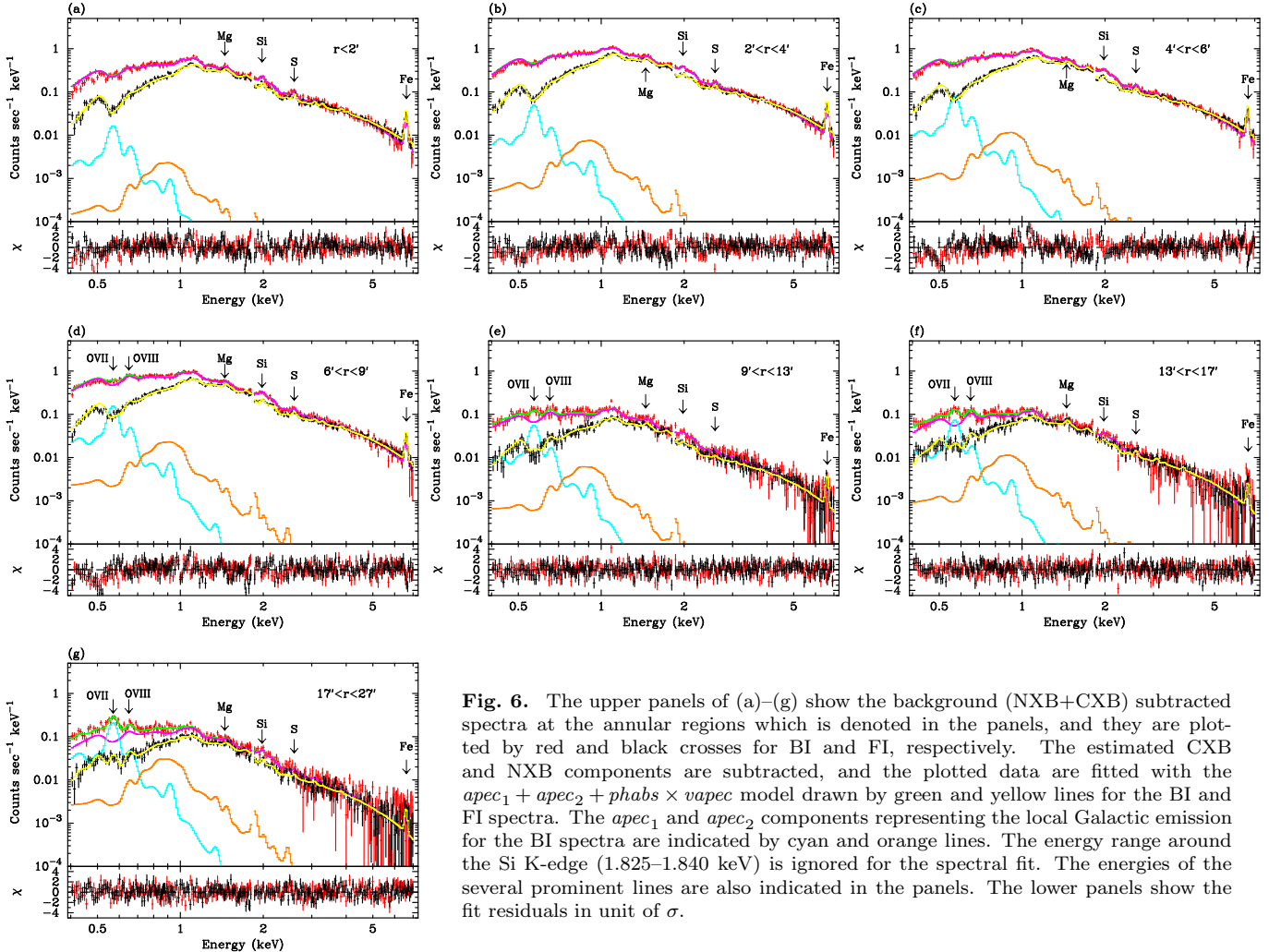


**Fig. 6.** The upper panels of (a)–(g) show the background (NXB+CXB) subtracted spectra at the annular regions which is denoted in the panels, and they are plotted by red and black crosses for BI and FI, respectively. The estimated CXB and NXB components are subtracted, and the plotted data are fitted with the  $apec_1 + apec_2 + phabs \times vapec$  model drawn by green and yellow lines for the BI and FI spectra. The  $apec_1$  and  $apec_2$  components representing the local Galactic emission for the BI spectra are indicated by cyan and orange lines. The energy range around the Si K-edge (1.825–1.840 keV) is ignored for the spectral fit. The energies of the several prominent lines are also indicated in the panels. The lower panels show the fit residuals in unit of  $\sigma$ .

We have confirmed that the assumed double- $\beta$  surface brightness profile is consistent with the observed Suzaku image by about  $\pm 15\%$  in figure 5 of Ishisaki et al. (2007). We further constrained that the surface brightness of the Galactic component (B) is nearly constant among all the extraction annuli, whereas its spectral shape is determined from the spectral fit of our Suzaku data. Details will be described in the next subsection.

We adopted the nominal Redistribution Matrix Files (RMF) of `ae_xiN_20060213.rmf` for spectral fitting, although slight degradation in energy resolution is expected (subsection 2.1). The ARFs were generated by “`xissimarfgen`”, and were convolved with the RMFs and added for three FI sensors, using the “`marfrmf`” and “`addrmf`” tasks in `Ftools`. The spectra from BI and FI are fitted simultaneously in the 0.4–7.1 keV band except for energy range of anomalous response around the Si K-edge (1.825–1.840 keV). We ignored below 0.4 keV because the C edge (0.284 keV) seen in the BI spectra could not be reproduced perfectly in our data. Energy range above 7.1 keV was also ignored because background Ni line ( $\sim 7.5$  keV) left artificial structures after the NXB subtraction at large radii. It is also known that the XIS response in  $E \gtrsim 8$  keV are not fully understood at the present stage. In the simultaneous fit of BI and FI, only the normalization are allowed to be different between them, although we found that the derived normalizations are quite consistent between the two.

#### 4.3. Estimation of Galactic Component

We found that the estimation of the Galactic component significantly affect the determination of the oxygen abundance, because both the ICM and the Galactic component contribute to the O VIII emission line (0.653 keV), and the XIS cannot resolve them by redshift due to the limited energy resolution. On the other hand, most of the O VII emission is supposed to originate in the Galactic component, because the ICM temperature  $kT \gtrsim 2$  keV  $\simeq 2.3 \times 10^7$  K is too high to emit the O VII lines (0.561, 0.568, 0.574 keV). See, e.g., figure 3 of Yoshikawa et al. (2003) for the oxygen line emissivity.

It is therefore important to estimate the Galactic component precisely, which is possible using the offset observation of A 1060 with Suzaku. In order to determine the surface brightness and the spectral shape of the Galactic component, we performed the simultaneous fit of the 13–17' and 17–27' annuli. The Galactic component is prominent in these annuli as shown in figure 6(f) and (g), however the ICM component is still dominant almost all the energy range except for the O VII line. We made the simultaneous fit in the whole 0.4–7.1 keV range (except 1.825–1.840 keV), assuming one or two *apec* models for the Galactic component, and the fit results are presented in table 5 and figure 7. The resultant normalization of the *apec* model in table 5 is scaled so that it gives the surface brightness in the unit solid angle of  $\text{arcmin}^2$ .

It may appear that the difference between these two models are not large in figure 7, however, it is notable that the derived O VIII line intensity for the Galactic compo-

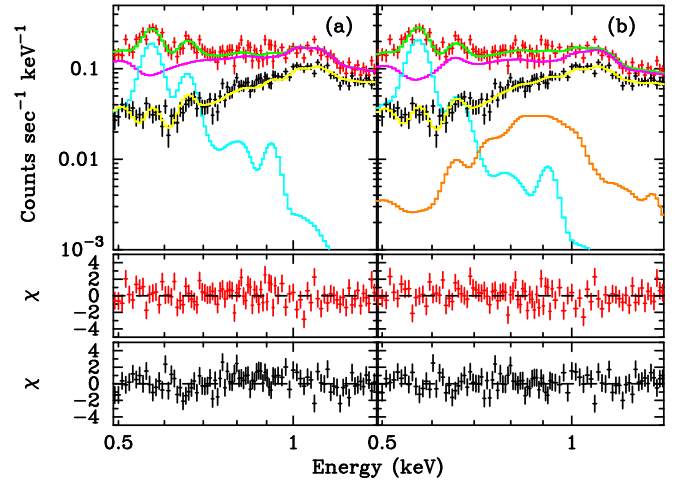


**Fig. 7.** (a) A magnification of 0.49–1.4 keV range of the BI (red) and FI (black) spectra in the 17–27' annulus. They are fitted with the  $apec_1 + phabs \times vapec$  model, and the best-fit model are drawn by green and yellow lines. The estimated CXB and NXB components were subtracted, and a simultaneously fit with the 13–17' annulus was conducted in the entire energy range of 0.4–7.1 keV. The  $apec_1$  or  $vapec$  component for BI is indicated by a cyan or magenta line, respectively. Lower two panels show the fit residuals for BI and FI in unit of  $\sigma$ . The orange dotted lines in figure 10 correspond to this modeling of the Galactic component. (b) Same as (a) but fitted with the  $apec_1 + apec_2 + phabs \times vapec$  model, and the  $apec_2$  component for BI is indicated by an orange line. We adopt this model in the spectral fit. See subsection 4.3 for details.

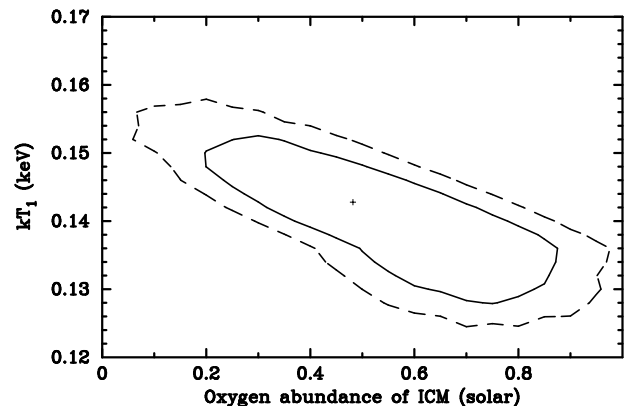


**Fig. 8.** A plot of confidence contour between  $kT_1$  (temperature of the cooler part of the two *apec* components) and the O abundance of *vapec* for the 17–27' annulus, in the simultaneous fitting of 13–17' and 17–27' annuli with the  $apec_1 + apec_2 + phabs \times vapec$  model. The cross denotes the best-fit location, and the two contours represent  $1\sigma$  and 90% confidence ranges, from inner to outer, respectively.

nent is by about twice larger for (a). We examined the improvement of the  $\chi^2$  ( $\Delta\chi^2 = 46$ ) with the  $F$ -test, and adding the  $apec_2$  component was justified with a large significance (false probability  $\sim 10^{-9}$ ). We further allowed the normalization of the  $apec_2$  to become free between the two annuli. The derived surface brightness ratio of the 13–17' annulus to 17–27' was  $0.9 \pm 0.2$ , hence it was consistent

**Table 5.** The best-fit parameters of the *apec* component(s) for the simultaneous fit of the spectra in 13–17′ and 17–27′ annuli.

Fit model	$Norm_1^*$	$kT_1$ (keV)	$Norm_2^*$	$kT_2$ (keV)	$\chi^2/\text{dof}$
(a) <i>apec</i> <sub>1</sub> + <i>phabs</i> × <i>vapec</i> .....	$1.20 \pm 0.07$	$0.179^{+0.006}_{-0.012}$	—	—	1128/994
(b) <i>apec</i> <sub>1</sub> + <i>apec</i> <sub>2</sub> + <i>phabs</i> × <i>vapec</i> .....	$1.66 \pm 0.35$	$0.143^{+0.014}_{-0.015}$	$0.21 \pm 0.05$	$0.737^{+0.063}_{-0.088}$	1082/992

\* Normalization of the *apec* component divided by the solid angle,  $\Omega^v = \pi \times (20')^2$ , assumed in the uniform-sky ARF calculation (20′ radius from the optical axis of each XIS sensor),  $Norm = \int n_e n_H dV / (4\pi(1+z)^2 D_A^2) / \Omega^v \times 10^{-20} \text{ cm}^{-5} \text{ arcmin}^{-2}$ , where  $D_A$  is the angular distance to the source.

to be constant. We also confirmed that the 9–13′ annulus gave the same result. We therefore concluded that the two *apec* models are required to account for the Galactic component. Hereafter, the *apec*<sub>1</sub> + *apec*<sub>2</sub> + *phabs* × *vapec* model are utilized for the spectral fitting, otherwise stated.

To demonstrate how sensitive the O abundance of the ICM is to the assumed Galactic component model, we present a confidence contour between  $kT_1$  (keV) of the *apec*<sub>1</sub> component and the O abundance (solar) of *vapec* for the outermost annulus (17–27′) in figure 8. There appears to exist a negative correlation between the two parameters, because higher temperature of the Galactic component produces more O VIII emission line relative to O VII, which contribute to reduce the O VIII line from the ICM (*vapec* component). Influences on the derived temperature and abundance by the modeling of the Galactic component will be tested in subsection 4.4, too.

In order to take into account both existence of the Galactic component itself and propagation of its statistical error, we simultaneously fitted each annulus with the outermost annulus of 17–27′. As mentioned in the previous subsection, the normalization of the *apec*<sub>1</sub> + *apec*<sub>2</sub> component are constrained to give the same surface brightness between the two annuli. The temperatures of the two *apec* models were also common between the two, however their values (two normalizations and two temperatures) themselves are left free. It is confirmed that the derived normalizations,  $Norm_1$  and  $Norm_2$ , and temperatures,  $kT_1$  and  $kT_2$ , are consistent with the values in table 5(b) within the quoted errors.

#### 4.4. Radial Temperature & Abundance Profiles

Before entering the spectral fit at each annulus, we investigate the fit result in the central 0–6′ region to test the capability in the abundance determination with the Suzaku XIS. This region exhibits nearly constant temperature and metal abundances (figure 10), and the contribution of the Galactic component is almost negligible (figure 6). The fit result is presented in table 6, in which most of element abundances are allowed to be free in the spectral fit, except for He, C, and N, which are fixed to 1 solar with the assumed abundance ratio of *anqr*.

Although the fit was not acceptable due mainly to the very high photon statistics than the systematic errors in the instrumental response, this result was useful to assess whether each element abundance was reasonably (sub-solar to  $\sim 2$  solar) determined or not. The Ar and Ca

abundances were reasonably determined although the errors are larger than other elements. We therefore decided to link the S, Ar, and Ca abundances to be the same, because they showed similar values. The Al abundance became 0.0, which is physically strange, therefore we fixed the Al abundance to 1 solar. The  $\chi^2/\text{dof}$  was increased to 1898/988 with this treatment, however we confirmed that other parameters did not change beyond the quoted error range in table 6. Somehow, the Ne and Ni abundances were larger than other elements. This might be due to these element lines could not be resolved from the Fe-L line complex. Note that the Ni abundance was also determined by Ni-L lines because we ignored energy range above 7.1 keV, while the Fe abundance was determined by both Fe-L and Fe-K lines. Anyway, we left these Ne and Ni abundances to move freely during the spectral fit. We also present results when the O, Ne, and Mg abundances are linked to have the same value in Appendix 2.

We also found that the assumed abundance table, which defines the “1 solar” of each element relative to H, significantly affects the determination of temperature and abundance. In fact, difference in the abundance table affects the fit results in three ways. Firstly, we assume the Galactic component to have the *apec*<sub>1</sub> + *apec*<sub>2</sub> model with “1 solar”. Secondly, the Galactic absorption model of *phabs* is also changed by the assumed abundance table. Lastly, the derived abundances are given in unit of “solar” by the *vapec* model. The first two effects are rather complicated, and details are investigated in Appendix 2. In this section, we treat only the solar abundance ratio of *anqr* (Anders & Grevesse 1989) with the *phabs* absorption model, simply because they are the *default standard* of XSPEC. In terms of the  $\chi^2$ , it appears to give the minimum  $\chi^2$  with the *lodd* (Lodders 2003) abundance table in combination with the *wabs* (Morrison & McCammon 1983) absorption model which utilizes the abundance table of *aneb* (Anders & Ebihara 1982) built-in the code (table 11).

We then examined the influence of uncertainty in the OBF contaminant using the spectrum within 6′. Figure 9(a) shows a magnification of the best-fit spectrum in the energy range of 0.4–1.0 keV with the “nominal” ARF response, in which transmission of the OBF contaminant was estimated according to the calibration files *ae\_xiN\_contami\_20060525.fits* ( $N=0,1,2,3$ ), as shown in figures 2 and 5(b). As described in subsection 4.2, the spectrum was simultaneously fitted with the 17–27′ annu-

**Table 6.** Result of the spectral fit in the central region of 0–6′, with the  $apec_1 + apec_2 + phabs \times vapec$  model. Only the parameters for the  $vapec$  component are presented. The abundance of each element (except for He, C, and N, which are fixed to 1 solar with the assumed abundance ratio of  $angr$ ) is allowed to be free in the spectral fit. Errors are 90% confidence range of statistical errors, and do not include systematic errors.

Region	$kT$ (keV)	O (solar)	Ne (solar)	Mg (solar)	Al (solar)	Si (solar)	$\chi^2/\text{dof}$
0–6′	$3.54^{+0.03}_{-0.03}$	$0.31^{+0.08}_{-0.08}$	$1.21^{+0.10}_{-0.10}$	$0.70^{+0.10}_{-0.09}$	$0.00^{+0.13}_{-0.00}$	$0.57^{+0.05}_{-0.05}$	1871/986
	<i>Norm</i> *	S (solar)	Ar (solar)	Ca (solar)	Fe (solar)	Ni (solar)	
	$302 \pm 3$	$0.57^{+0.07}_{-0.07}$	$0.53^{+0.16}_{-0.16}$	$0.44^{+0.17}_{-0.17}$	$0.43^{+0.01}_{-0.01}$	$0.83^{+0.23}_{-0.23}$	

\* Normalization of the  $vapec$  component scaled with a factor of  $\text{SOURCE\_RATIO\_REG} / \text{AREA}$  in table 4,

$Norm = \frac{\text{SOURCE\_RATIO\_REG}}{\text{AREA}} \int n_e n_H dV / (4\pi(1+z)^2 D_A^2) \times 10^{-20} \text{ cm}^{-5} \text{ arcmin}^{-2}$ , where  $D_A$  is the angular distance to the source.

**Table 7.** Results of the spectral fits in the central region of 0–6′ by changing the amount of the OBF contaminant.

Contaminant	O (solar)	Ne (solar)	Mg (solar)	Al (solar)	Si (solar)	S (solar)	Ar (solar)	Ca (solar)	Fe (solar)	Ni (solar)
nominal	0.31	1.21	0.70	0.00	0.57	0.57	0.53	0.44	0.43	0.83
+20%	0.43	1.05	0.48	0.00	0.47	0.50	0.45	0.46	0.41	0.41
free *	0.38	1.12	0.57	0.00	0.51	0.53	0.47	0.43	0.42	0.54
Contaminant	$kT$ (keV)	<i>Norm</i> †	$kT_1$ (keV)	<i>Norm</i> <sub>1</sub> ‡	$kT_2$ (keV)	<i>Norm</i> <sub>2</sub> ‡	$N_{\text{CO}_{1/6}}$ § BI	FI	$\chi^2/\text{dof}$	
nominal	3.54	302	0.159	1.00	0.752	1.00	1.74	2.32	1878/986	
+20%	3.36	298	0.148	1.40	0.721	1.09	2.11	2.72	1746/986	
free *	3.50	301	0.159	0.96	0.765	0.95	2.18	2.38	1681/982	

\* We fitted the amount of the OBF contaminant as a free parameter with the C/O number ratio fixed to 6.

† Normalization of the  $vapec$  model, calculated in the same way with table 6

‡ Ratio to the normalization of the “nominal” ARF.

§ Column density of the OBF contaminant with chemical composition of  $\text{CO}_{1/6}$  for BI and FI in unit of  $10^{18} \text{ cm}^{-2}$ .

**Table 8.** Summary of the best-fit parameters of the  $vapec$  component for each annular region with the  $apec_1 + apec_2 + phabs \times vapec$  model. Each annulus is simultaneously fitted with the the outermost 17–27′ annulus. Errors are 90% confidence range of statistical errors, and do not include systematic errors. The solar abundance ratio of  $angr$  is assumed. These results are plotted in figure 10. The O abundance in the outer two regions becomes lower when the Galactic component is expressed by a single  $apec$  model, which is drawn by orange dotted lines in figure 10. The  $kT$ , O, and Mg columns at  $r < 6′$  are slightly different when the OBF contaminant is increased by “+20%”, which is drawn by black dotted lines in figure 10. The Ne abundance is probably not reliable because the Suzaku XIS cannot resolve the ionized Ne lines from the Fe-L line complex.

Region	<i>Norm</i> *	$kT$ (keV)	O (solar)	Ne (solar)	Mg (solar)	Si (solar)	S, Ar, Ca (solar)	Fe (solar)	Ni (solar)	$\chi^2/\text{dof}$
0–2′	$605 \pm 12$	$3.34^{+0.04}_{-0.04}$	$0.38^{+0.16}_{-0.15}$	$1.20^{+0.20}_{-0.20}$	$0.76^{+0.19}_{-0.19}$	$0.69^{+0.11}_{-0.11}$	$0.82^{+0.12}_{-0.12}$	$0.49^{+0.03}_{-0.03}$	$1.13^{+0.46}_{-0.45}$	1240/992
2–4′	$352 \pm 5$	$3.39^{+0.03}_{-0.03}$	$0.28^{+0.11}_{-0.12}$	$1.11^{+0.16}_{-0.15}$	$0.65^{+0.14}_{-0.14}$	$0.52^{+0.08}_{-0.08}$	$0.52^{+0.08}_{-0.08}$	$0.42^{+0.02}_{-0.02}$	$0.90^{+0.34}_{-0.34}$	1290/992
4–6′	$198 \pm 3$	$3.42^{+0.04}_{-0.04}$	$0.29^{+0.13}_{-0.13}$	$1.24^{+0.18}_{-0.16}$	$0.67^{+0.15}_{-0.15}$	$0.58^{+0.09}_{-0.09}$	$0.53^{+0.09}_{-0.10}$	$0.41^{+0.02}_{-0.02}$	$0.87^{+0.38}_{-0.37}$	1345/992
6–9′	$109 \pm 2$	$3.25^{+0.04}_{-0.04}$	$0.58^{+0.14}_{-0.14}$	$1.17^{+0.16}_{-0.15}$	$0.59^{+0.15}_{-0.15}$	$0.50^{+0.08}_{-0.08}$	$0.55^{+0.09}_{-0.09}$	$0.40^{+0.02}_{-0.02}$	$1.17^{+0.36}_{-0.35}$	1329/992
9–13′	$44 \pm 2$	$2.87^{+0.10}_{-0.10}$	$0.65^{+0.34}_{-0.29}$	$0.89^{+0.35}_{-0.33}$	$0.75^{+0.33}_{-0.32}$	$0.27^{+0.17}_{-0.17}$	$0.19^{+0.20}_{-0.19}$	$0.40^{+0.05}_{-0.05}$	$1.13^{+0.77}_{-0.72}$	1057/992
13–17′	$26 \pm 1$	$2.50^{+0.09}_{-0.09}$	$0.72^{+0.29}_{-0.38}$	$0.44^{+0.29}_{-0.28}$	$0.78^{+0.29}_{-0.27}$	$0.30^{+0.15}_{-0.14}$	$0.44^{+0.18}_{-0.17}$	$0.25^{+0.05}_{-0.05}$	$0.16^{+0.60}_{-0.16}$	1082/992
17–27′	$13 \pm 1$	$2.22^{+0.11}_{-0.12}$	$0.48^{+0.41}_{-0.37}$	$0.30^{+0.29}_{-0.26}$	$0.21^{+0.22}_{-0.21}$	$0.28^{+0.12}_{-0.12}$	$0.21^{+0.14}_{-0.14}$	$0.21^{+0.04}_{-0.04}$	$0.00^{+0.41}_{-0.00}$	—†

\* Normalization of the  $vapec$  model, calculated in the same way with table 6.

† The 17–27′ annulus was fitted simultaneously with other annuli, and the best-fit values with the 13–17′ annulus are presented here.

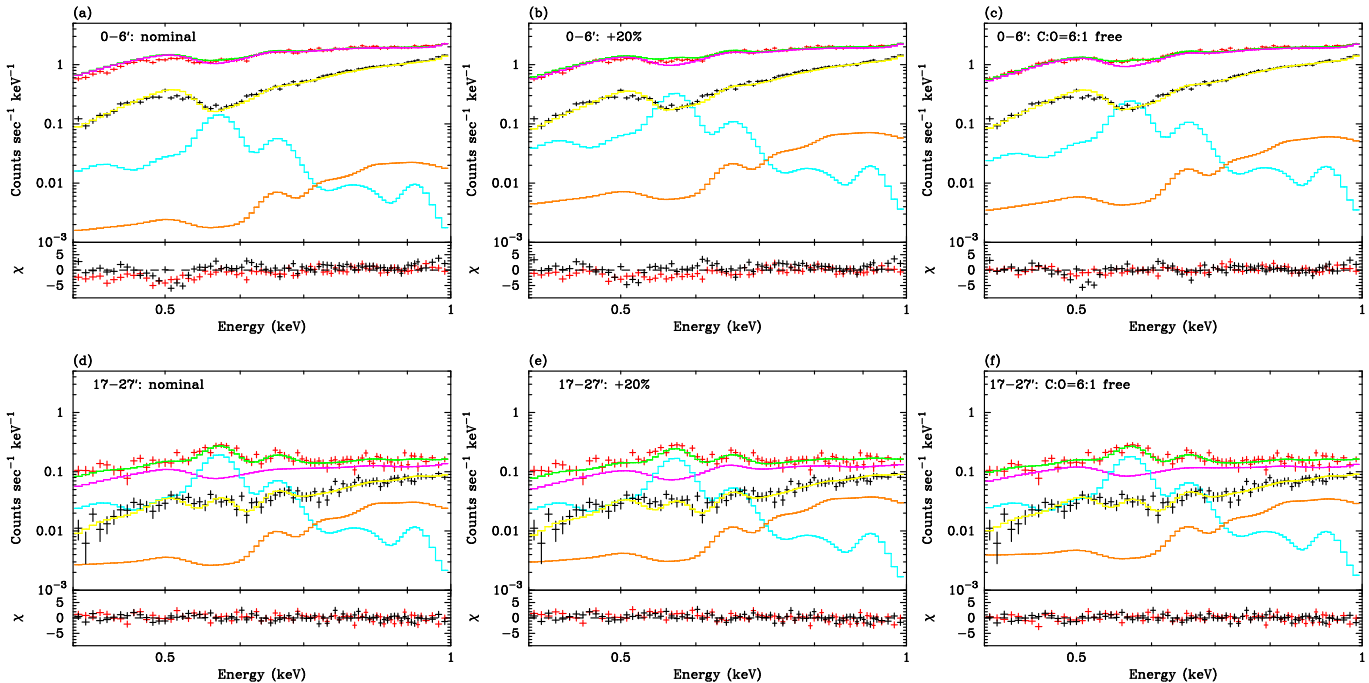


**Fig. 9.** (a) A magnification of the best-fit spectrum at 0–6′ annulus in the energy range of 0.4–1.0 keV with the “nominal” ARF response, in which transmission of the OBF contaminant was estimated according to the calibration files `ae_xiN_contami_20060525.fits` ( $N = 0, 1, 2, 3$ ). Table 6 and the “nominal” row of table 7 show the best-fit parameters. (b) The best-fit spectrum with the “+20%” ARF, in which amount of the OBF contaminant was increased by +20% than the “nominal” ARF. The “+20%” row of table 7 shows the best-fit parameters. (c) The best-fit spectrum with the no-contaminant ARF but fitted with *varabs* × (*apec*<sub>1</sub> + *apec*<sub>2</sub> + *phabs* × *vapec*) model to consider the transmission of the OBF contaminant in the XSPEC *varabs* model with chemical composition of  $\text{C O}_{1/6}$ . The “free” row of table 7 shows the best-fit parameters. (d), (e), (f) Same as (a), (b), (c) but for the 17–27′ annulus, respectively. Each spectrum was simultaneously fitted with (a), (b), (c).

lus shown in figure 9(d). In this figure, it is suggested that the absorption in the low energy band is slightly inconsistent between BI and FI sensors, namely, the BI spectrum appears to need more absorption in 0–6′ where the amount of contamination is larger than 17–27′ (see figure 2). We also found that the contamination measurement by RXJ1856.5–3754 on October 25, 2005 in the XIS hardware paper (figure 14 of Koyama et al. 2006) indicates by about 20% larger amount of the OBF contaminant than the “nominal” value for BI (XIS1).

We therefore generated ARF responses changing the amount of the OBF contaminant by +20%. The fit result is shown in figure 9(b), (e) and table 7 (“+20%” row). Note that the CXB background to subtract was also modified in this fit. The fit residual for 0–6′ was improved, and the  $\chi^2$  was decreased by  $\Delta\chi^2 = 132$ . We further tested the fit by adding an absorption of the OBF contaminant with chemical composition of  $\text{C O}_{1/6}$  to the fit model using the XSPEC *varabs* model.<sup>2</sup> The fit result is shown in figure 9(c) and (f). The best-fit values are summarized in table 7 (“free” row), and the  $\chi^2$  was improved by  $\Delta\chi^2 = 197$ . The derived amount of contaminant for BI was by 25% larger than the “nominal” value, and by 3% larger for FI. We think that the deviation

from the “nominal” value for BI is beyond the calibration uncertainty, however, almost all of the best-fit values at the “free” row in table 7 are between values at “nominal” and “+20%”. We therefore consider the +20% result as the systematic error range due to the uncertainty in the OBF contaminant.

Considering these systematics, results of the spectral fit at each annulus are summarized in table 8 and figure 10. We tested the results by changing the background normalization by  $\pm 10\%$ , and they are plotted in green dotted lines in figure 10. The systematic error due to the background estimation is almost negligible. Difference in the best-fit values by modeling the Galactic component with a single *apec* was investigated, and they were indicated by orange dotted lines. The differences are within the statistical error for the inner five annuli, however, O abundance becomes lower than the 90% confidence error at the outer two annuli as indicated in figure 7, and temperature and Fe abundance become lower at the outermost annulus. This is due mainly to the fact that the XIS cannot resolve the ICM O VIII line from the Galactic O VIII by redshift. The systematic error range due to the uncertainty in the OBF contaminant is indicated by black dotted lines. It is sometimes larger than the statistical errors at small radii ( $r \lesssim 6'$ ), particularly for  $kT$ , O, and Mg abundances. Though Ne abundance is significantly larger than other elements at small radii ( $r < 9'$ ), it is probably

<sup>2</sup> In this method, we used the same CXB background with the “nominal” ARF, and the surface brightness of the Galactic component was slightly different between 0–6′ and 17–27′.

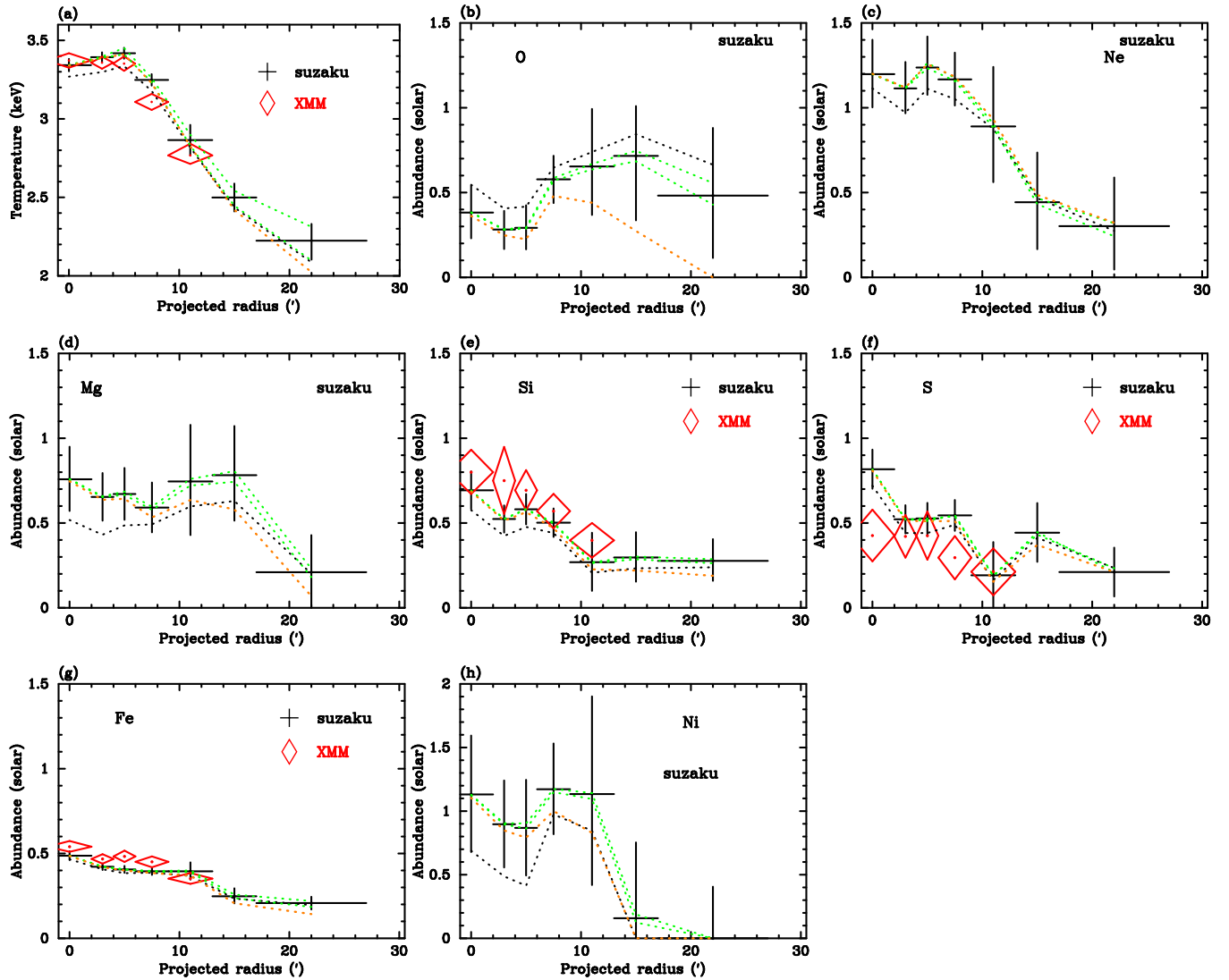


Fig. 10. (a) Radial temperature profiles derived from spectral fit of the Suzaku (black) and XMM-Newton (red) spectra at each annulus. The horizontal axis denotes the projected radius and deprojection are not conducted. The same data with table 8 are used for Suzaku. The black dotted lines correspond to shifts of the best-fit values by changing thickness of the OBF contaminant by  $\pm 20\%$ . The green dotted lines denote those when the estimated CXB and NXB levels are changed by  $\pm 10\%$ . The orange dotted line shows the best-fit value when the Galactic component is modeled by a single *apec*. Regarding XMM-Newton, the *phabs*  $\times$  *vapcc* model are used for the spectral fit, and the O, Ne, Mg, and Ni abundances are fixed to 1 solar in the assumed abundance table of *angr*. (b)–(h) Radial abundance profiles derived and plotted in the same way as (a).

not reliable because the Suzaku XIS cannot resolve the ionized Ne lines from the Fe-L line complex.

We also plot the XMM-Newton results for the inner five annuli with red diamonds, in which the *phabs*  $\times$  *vapcc* model are used for the spectral fit, and the Ne, Ar, Ca and Ni abundances are fixed to 1 solar. Namely, the Galactic component is ignored. They are almost consistent with the Suzaku results, although XMM-Newton appears to give slightly higher abundance for Fe and Si, while lower abundance for S.

#### 4.5. Direct Comparison of O VII and O VIII Intensities

We also investigated the surface brightness of the O VII and O VIII emission lines in order to estimate the O abundance of the ICM directly from the line intensities. The

surface brightness of the O VII and O VIII were derived by fitting the annular spectrum with a *power-law* + *gaussian* + *gaussian* model. In the fitting, we fixed the Gaussian  $\sigma$  to be 0, and allowed the energy center of the two Gaussians to vary within 555–573 eV or 648–658 eV for O VII or O VIII, respectively. The derived line intensities are summarized in table 9 and figure 11(a). There is a clear excess of the O VIII intensity towards the cluster center, while O VII is consistent with constant. This is a strong evidence that the O VIII emission is associated with the ICM itself, on the other hand, O VII might be due mainly to the Galactic origin.

We compared the surface brightness of the oxygen lines with that at a neighbor of A 1060, the NGC 2992 field. Though NGC 2992 is located at  $18^\circ$  offset from A 1060,

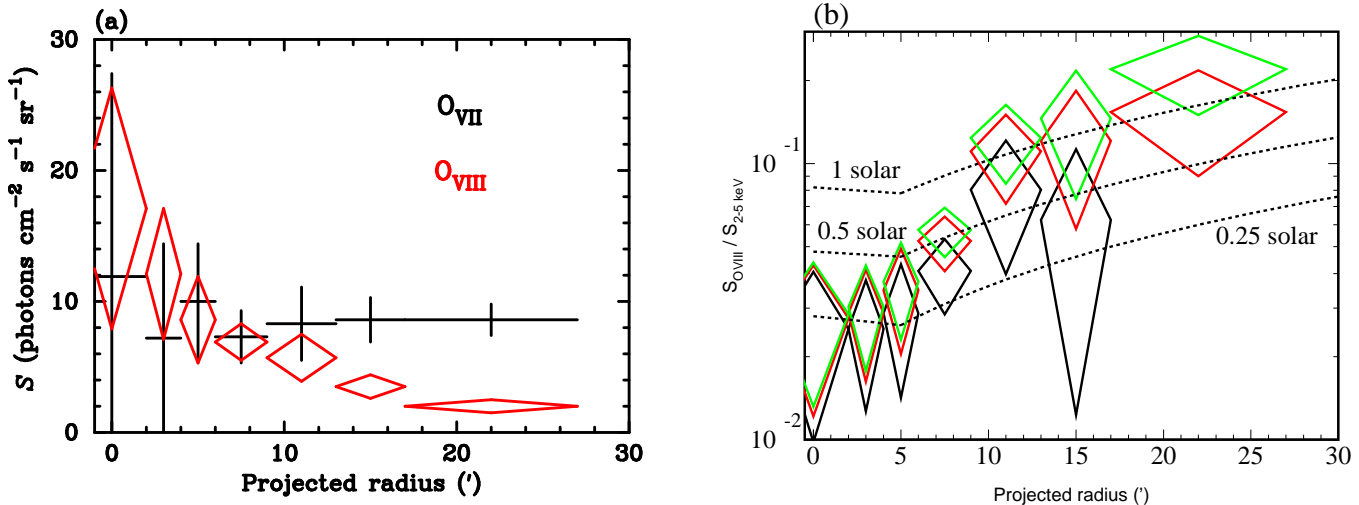


**Fig. 11.** (a) Line intensities of O VII and O VIII at each annulus of A 1060 in unit of photons  $\text{cm}^{-2} \text{s}^{-1} \text{sr}^{-1}$ . Each value is shown in table 9. (b) The O VIII emission line intensities in table 9 divided by the surface brightness of the 2–5 keV continuum are plotted in green diamonds against the radius of each annulus. The red or black diamonds correspond to the ratios when the O VIII intensities of the NGC 2992 field or the outermost annulus (17–27′) are subtracted as an offset. Dashed lines represent expected ratios for the *vapex* model with 0.25, 0.5, and 1 solar abundances, assuming the observed temperature at each annulus (table 8).

**Table 9.** Line intensities of O VII and O VIII at each annulus of A 1060 and the NGC 2992 field in unit of photons  $\text{cm}^{-2} \text{s}^{-1} \text{sr}^{-1}$ . These intensities are derived from the spectral fit with *power-law + gaussian + gaussian* model (see figure 12 for the NGC 2992 field), assuming the uniform-sky ARF response. Intensities by McCammon et al. (2002) measured with a high resolution microcalorimeter array for a large sky area of  $\sim 1$  sr are also presented.

Region	O VII	O VIII
A 1060 center (0–2′) .....	$11.9^{+15.5}_{-11.9}$	$17.1 \pm 9.2$
A 1060 center (2–4′) .....	$7.2 \pm 7.2$	$12.1 \pm 5.0$
A 1060 center (4–6′) .....	$10.0 \pm 4.4$	$8.6 \pm 3.3$
A 1060 center (6–9′) .....	$7.3 \pm 2.0$	$6.9 \pm 1.4$
A 1060 offset (9–13′) .....	$8.3 \pm 2.8$	$5.7 \pm 1.8$
A 1060 offset (13–17′) .....	$8.6 \pm 1.7$	$3.5 \pm 0.9$
A 1060 offset (17–27′) .....	$8.6 \pm 1.2$	$2.0 \pm 0.5$
NGC 2992 field .....	$4.1 \pm 0.6$	$0.6 \pm 0.2$
McCammon et al. (2002) .....	$4.8 \pm 0.8$	$1.6 \pm 0.4$

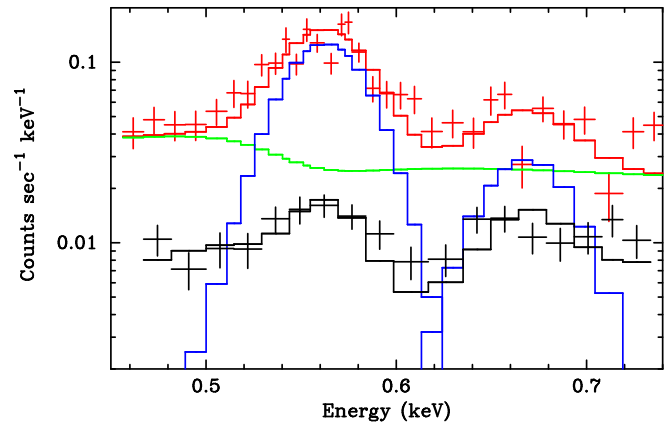


**Fig. 12.** The 0.46–0.74 keV spectra of the NGC 2992 field with BI (red) and FI (black) are fitted with the *power-law + gaussian + gaussian* model. The red and black lines represent the best-fit model, and the model components for BI are plotted by green (*power-law*) and blue (two *gaussian*) lines. The central energies of two Gaussians are constrained to be within  $\pm 5$  eV range of O VII and O VIII lines, and  $\sigma$  of Gaussians are fixed to 0.0.

the Galactic latitude of A 1060 and NGC 2992 is similar (table 1), and the neutral hydrogen column density ( $N_{\text{H}} = 5.1 \times 10^{20} \text{cm}^{-2}$ ; Dickey & Lockman 1990) is comparable to A 1060. NGC 2992 ( $z = 0.007710$ ) has an active galactic nuclei, which is expected to emit no oxygen lines. In addition, we excluded the main target with a radius of 5′ centered on NGC 2992, and utilized the outer region for the spectral analysis in figure 12.

The surface brightness of the O VII and O VIII emissions in the outermost annulus of the A 1060 observation was roughly twice larger than the NGC 2992 field. Line intensities by McCammon et al. (2002) measured with a high resolution microcalorimeter array for a large sky area of  $\sim 1$  sr are also presented in table 9, and the O VIII intensity was consistent with the outermost annulus (17–27′)

of the A 1060. It is suggested that both the O VII and O VIII lines in our observation are somewhat mixture of the ICM and the Galactic origin. However, we could not confirm excess O VII emission towards the cluster center, we concentrate on the O VIII emission.

Then we calculated the surface brightness ratio of the O VIII line divided by the 2–5 keV continuum at each annulus, as presented in figure 11(b) by green diamonds. Here, we subtracted the O VIII intensity at the NGC 2992 field (red diamonds) or the intensity at the outermost annulus (black diamonds), as an “offset” due to the Galactic component. The dashed lines represent the calculated ratio by the XSPEC simulation fixing the O abundance of

ICM to 0.25, 0.5, and 1 solar. The ICM temperature at each annulus is assumed to have the measured value in figure 10(a). Actual value of the O abundance is supposed to lie between the black and green diamonds. The radial O abundance profile obtained in figure 10(b) is mostly consistent with this plot.

#### 4.6. Central Cool Component of A 1060

Chandra observation resolved two central elliptical galaxies of A 1060, NGC 3311 and NGC 3309 (Yamasaki et al. 2002). We estimated the flux of an additional cool component for the central galaxies with the *vap*ec model of  $kT = 0.8$  keV and 0.5 solar abundance at  $z = 0.0114$ , and obtained an upper limit (90% confidence level) to be  $L_X = 5.2 \times 10^{40}$  erg s $^{-1}$  (0.4–4.5 keV) in the central region within  $r < 2'$ . In this fit, temperatures of the Galactic components (two *ap*ec) were fixed at 0.146 and 0.662 keV, and only the ICM component was allowed to be free. This upper limit is consistent with the sum of the ISM flux of the two elliptical galaxies by Yamasaki et al. (2002),  $L_X = (1.8 \pm 0.6) \times 10^{40}$  erg s $^{-1}$  (0.4–4.5 keV).

## 5. Discussion

### 5.1. Temperature Profile

The temperature in A1060 observed with Suzaku shows a decline from  $\sim 3.4$  keV in the central region ( $r \lesssim 5' \sim 70$  kpc) to  $\sim 2.2$  keV in the outermost annulus of  $17\text{--}27' \sim 240\text{--}380$  kpc  $\sim 0.16\text{--}0.25 r_{180}$ . This feature is roughly consistent with the previous result for the inner region ( $r < 13'$ ) measured with XMM-Newton (Hayakawa et al. 2006), although our Suzaku result indicate slight flattening of the temperature profile in the outer annuli. Hayakawa et al. (2006) suggested a faster decline of the temperature profile of A 1060 than the average  $T/\langle T \rangle$  curve by Markevitch et al. (1998) obtained from 30 nearby clusters (excluding A 1060) with ASCA observations. However, now it appears to become consistent with them by taking the emission-weighted average temperature,  $k\langle T \rangle = 2.5$  keV.

Recent measurements of 13 nearby relaxed clusters (excluding A 1060) with Chandra by Vikhlinin et al. (2005) showed that the temperature reaches at a peak at  $r \sim 0.15 r_{180}$  and then declines to  $\sim 0.5$  of its peak value at  $r \simeq 0.5 r_{180}$ , in good agreement with Markevitch et al. (1998). They also found that clusters whose temperature profiles peak at  $r < 70$  kpc  $\ll 0.15 r_{180}$  (MKW4 and RX J1159+5531) shows a larger peak-temperature-ratio of  $T_p/\langle T \rangle \sim 1.35$ . This is exactly the case of A 1060, which shows the peak-temperature of  $kT_p = 3.42 \pm 0.04$  keV at  $r = 4\text{--}6' \sim 70$  kpc with our Suzaku measurement. Using the relation of  $T_p/\langle T \rangle \sim 1.35$ , the emission-weighted average temperature is calculated to be  $k\langle T \rangle = 2.5$  keV, as suggested in the previous paragraph. These three correspond to clusters without cooling core, hence this apparent steep temperature decline at  $r \lesssim 0.2 r_{180}$  might be a common feature for the non-cooling flow clusters.

In order to determine actual value of  $k\langle T \rangle$  for A 1060, further offset observations toward  $r_{180} \sim 110'$  are required. Since the wide and energy-dependent point-spread func-

tion of ASCA tended to give a flatter temperature profile for A 1060 (Tamura et al. 1996; Furusho et al. 2001), studies of the  $T/\langle T \rangle$  curve in cluster outskirts with Suzaku will be useful to look at the true temperature features.

Dolag et al. (2004) conducted a smoothed particle hydrodynamics (SPH) simulation to reconstruct the structure of the Local Universe, which well reproduces the position, mass, and temperature of A 1060 (“Hydra” of table 1 in Yoshikawa et al. 2004). The simulated temperature of A 1060 was 3.4 keV within  $r < 20' \sim 0.18 r_{180}$ . The radial temperature profile of simulated A 1060 is presented by Kawahara et al. (2007), based on the updated version of the SPH simulation by Dolag et al. (2005). It reproduces the shape of the temperature profile obtained with our Suzaku observation pretty well, although the temperature in the simulation is higher than our observation. This is partly because our temperature profile in figure 10(a) is plotted against the projected radius, in which the ICM emission is integrated along the line of sight, while the simulated temperature is plotted against the spherical radius. It is pointed out that the spectroscopic temperature in the real X-ray observation tend to give lower temperature than the emission-weighted temperature calculated in the simulation due to the multi-phase nature of the ICM not only from the radial profiles but also from the local inhomogeneities (Mazzotta et al. 2004; Kawahara et al. 2007).

There is a small flat-top in the observed temperature profile within  $r \lesssim 5' \sim 70$  kpc in figure 10(a). This feature might indicate an initial phase in the formation of cooling core. The SPH simulation predicts that the period of the last major merger occurred at an age of  $\sim 3$  Gyr ago ( $z \sim 0.3$ ). This implies that the temperature flat-top has been made within recent  $\sim 3$  Gyr. The thermal conduction length scale is calculated as

$$r_{\text{cond}} = 155 \left( \frac{t_{\text{cond}}}{3 \text{ Gyr}} \right)^{\frac{1}{2}} \left( \frac{n_e}{0.01 \text{ cm}^{-3}} \right)^{-\frac{1}{2}} \left( \frac{kT}{3 \text{ keV}} \right)^{\frac{5}{4}} \text{ kpc},$$

where  $t_{\text{cond}}$  is the thermal conduction time,  $n_e$  is the electron density, assuming the classical Spitzer conductivity. This length scale is similar to the size of the flat-top.

In subsection 4.6, only an upper limit of  $5 \times 10^{40}$  erg s $^{-1}$  for the cool component in the ICM was obtained. It confirms that the sharp cusp structure in the Chandra image of A1060 (Hayakawa et al. 2004) really reflects the gravitational mass concentration and does not come from cool gas of high emissivity.

### 5.2. Abundance Profiles

In this paper, we obtained emissivity weighted abundance profiles of Ni, Fe, Si, S, Mg, Ne and O in the ICM of A 1060 up to a radius of  $27' \simeq 380$  kpc, although Ni and Ne abundances are not reliable due to the strong and complex Fe-L line emissions. Abundances of Si, S, and Fe decrease from  $\sim 0.7, 0.8$  and  $0.5$  solar in the central region, to  $\sim 0.3, 0.2$  and  $0.2$  solar, respectively, in the outskirts of the cluster. De Grandi & Molendi (2001) showed that non-cooling flow clusters do not exhibit a steep abundance gradient due possibly to disruption of the central

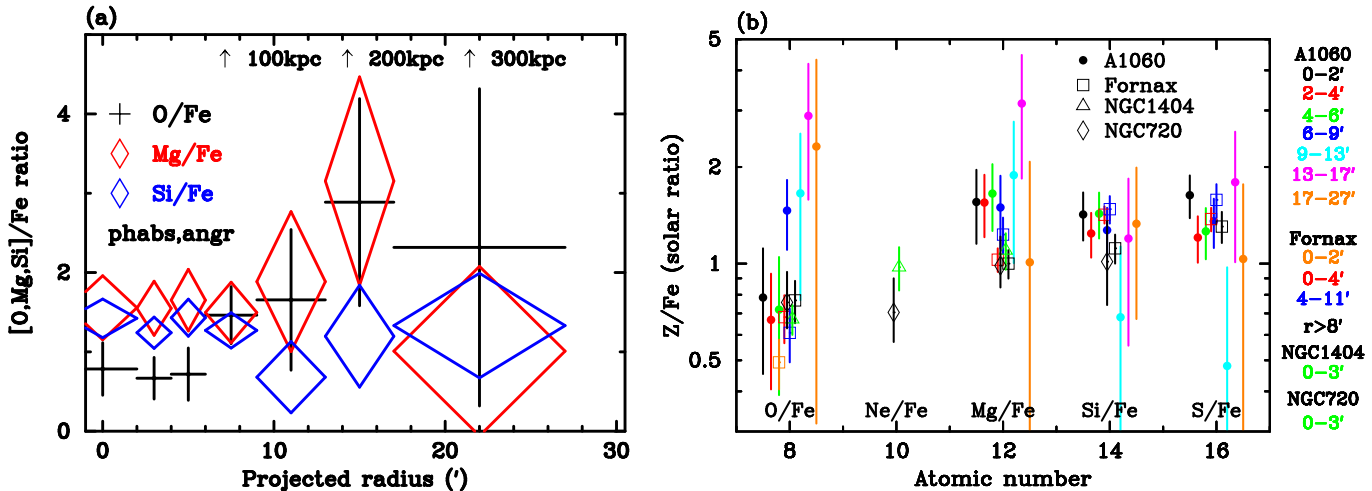


Fig. 13. (a) Abundance ratios of O (black), Mg (red) and Si (blue) divided by Fe. (b) Abundance ratios of O, Ne, Mg, Si, and S, divided by Fe for Fornax cluster, NGC 1404 (Matsushita et al. 2007a), NGC 720 (Tawara et al. 2007), and A 1060. In both plots, the solar abundance ratio of *anqr* (Anders & Grevesse 1989) is assumed, and only the statistical errors are plotted.

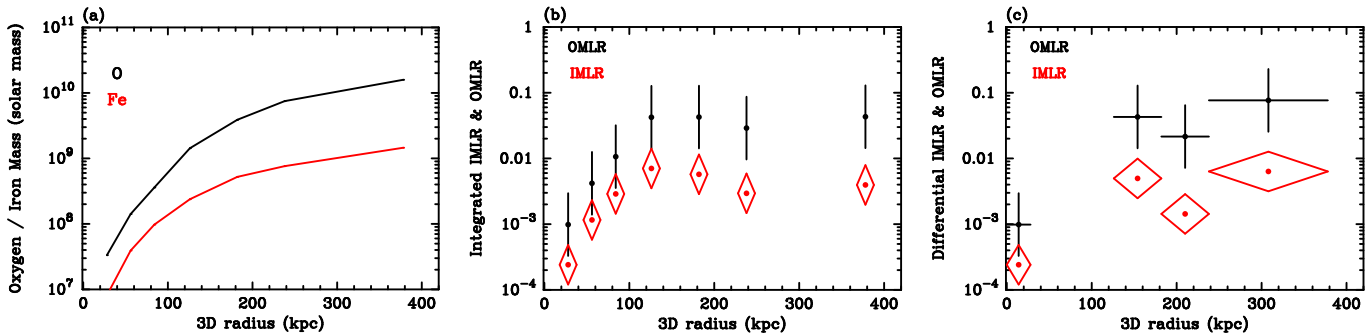


Fig. 14. (a) Cumulative Fe (red) and O (black) mass profiles of A 1060. (b) Integrated iron mass-to-light ratio (IMLR) and oxygen mass-to-light ratio (OMLR) in unit of  $M_{\odot}/L_{\odot}$  in the blue band. (c) Differential IMLR and OMLR calculated at each annulus. The annular range of 2–9' are not plotted because there are no member galaxies cataloged by Christlein & Zabludoff (2003). See text subsection 5.3 for details.

cool cores after major merger events. A 1060 shows clear gradients for Fe, Si, and S, although it is a very relaxed system without the cD galaxy and cooling core.

The other elements, Mg and O, show somewhat flatter radial distributions. The measured Mg abundance is consistent with constant up to the 13–17' annulus, namely out to 240 kpc from the cluster center. Oxygen also exhibits a flat distribution or a slight increase at  $r \simeq 10'$ . We have to note that the O abundances depend on the estimation of the Galactic component as described in subsection 4.3. The O abundance in the outer annuli is particularly affected by the surface brightness and temperature of the cooler Galactic component ( $kT_1 \sim 0.15$  keV). The O and Mg abundances at  $r \lesssim 6'$  are also affected by the uncertainties in the OBF contaminant (subsection 4.4). We have tried to take into account all the possible systematic errors, and the results are presented in figure 10. In addition, systematic effects caused by the definition of the solar abundances were addressed and described in appendix 2.

In order to compare the relative variation in the abun-

dance profiles, we show abundance ratios of O, Mg, and Si divided by Fe as a function of projected radius in figure 13(a). Apparently, the profiles of Si/Fe, O/Fe, and Mg/Fe show different gradients. The Si/Fe ratio is consistent with a constant value, while the O/Fe and Mg/Fe ratios seem to increase with radius excluding the outermost annulus (17–27'). This trend is similar when the O, Ne, and Mg abundances are constrained to have the same values in different solar units in figure 19(c).

Recent Suzaku observations also showed the O and Mg abundances in poorer systems: an elliptical galaxy NGC 720 (Tawara et al. 2007), the Fornax cluster, and NGC 1404 (Matsushita et al. 2007a). The Fe ratios of elements for these systems are compared in figure 13(b). The ratios Si/Fe and S/Fe are almost the same with A 1060 in other systems. Somehow, the Mg/Fe ratio in A 1060 is  $\sim 50\%$  higher than those in other systems. However, if one considers the influence of the OBF contaminant, this ratio can drop and the difference becomes insignificant. Abundance ratio of O/Fe shows almost the same values with A 1060 at their centers, and in the outer regions

**Table 10.** Comparison of IMLR and OMLR with other systems.

	IMLR	OMLR	$< r$	$kT$	Reference
NGC 720 .....	$1 \times 10^{-4}$	$4 \times 10^{-4}$	25 kpc	$\sim 0.56$ keV	Tawara et al. (2007)
Fornax .....	$4 \times 10^{-4}$	$2 \times 10^{-3}$	130 kpc	$\sim 1.3$ keV	Matsushita et al. (2007a)
Centaurus .....	$4 \times 10^{-3}$	$3 \times 10^{-2}$	190 kpc	$\sim 4$ keV	Matsushita et al. (2007b)
A 1060 .....	$4.0 \times 10^{-3}$	$4.3 \times 10^{-2}$	380 kpc	$\sim 3$ keV	This work

A 1060 indicates a higher value than others.

This peculiar behavior of the O/Fe ratio has been reported by Tamura et al. (2004) with XMM-Newton as an average of 19 clusters which are mainly composed of X-ray bright and relaxed clusters with a cD galaxy (excluding A 1060). The O/Fe ratio is  $\sim 0.7$  solar within  $r \lesssim 50$  kpc, which increases to  $\sim 1.5$  solar at  $r \sim 100$  kpc, and more at  $r \gtrsim 200$  kpc, in figure 5(b) of Tamura et al. (2004), assuming the solar abundance ratio of *angr* (Anders & Grevesse 1989). This is much alike the O/Fe plot in figure 13(a).

Since these differences are not simply explained by the ion mass, we need to consider that the enrichment processes have a significant difference between O and Fe, for example. It is generally considered that enrichment of O and other SN II originated metals has occurred in the early stage of cluster formation, certainly before the last merger epoch. The relatively flat distributions of O and Mg indicate that the early metal enrichment has caused these features. One plausible explanation is the enrichment in the form of starburst-driven galactic winds (e.g. Strickland & Stevens 2000). Recent numerical simulation of the cluster metal enrichment indicates that even a metallicity peak in an intermediate radius can be created by enrichment through galactic winds (Kepferer et al. 2006, priv. comm.), which resembles our oxygen feature.

The other possibility is the early metal enrichment by massive Population III stars (e.g. Matteucci et al. 2006) In this case, a large fraction of the intergalactic space would be enriched with metals. One big riddle in the obtained abundance profiles is that the Mg abundance at the central region appears to be significantly higher than the O abundance, although both O and Mg are mainly produced by SN II. Loewenstein (2001) suggests that pre-enrichment by a generation of massive Population III stars may account for the abundance anomalies of O, Si, and Fe observed in the ICM. However, Yoshida et al. (2004) concluded that metals originating from the earliest generation of stars cannot be responsible for the observed abundance anomalies in the ICM. Future quantitative studies of metal abundances in the outer regions ( $\sim r_{180}$ ) or even outside of clusters will be important to locate the origin of metals. Instruments with much higher energy resolution such as microcalorimeters will be desired for these studies.

### 5.3. IMLR and OMLR

Combining the X-ray luminous gas mass profile by Hayakawa et al. (2006) with XMM-Newton and the abundance profiles obtained with Suzaku, we calculated the cumulative iron or oxygen mass profiles in figure 14(a).

Strictly speaking, the abundance profile is derived from the projected spectrum along the line of sight, we approximated it to the spherical distribution. The iron and oxygen mass within  $r \lesssim 380$  kpc is calculated to be  $\sim 1.4 \times 10^9 M_\odot$  and  $1.6 \times 10^{10} M_\odot$ , respectively.

Based on the member galaxy catalog (69 galaxies within the projected radius,  $r < 27' \sim 380$  kpc) by Christlein & Zabludoff (2003), we also calculated the iron mass-to-light ratio (IMLR) and oxygen mass-to-light ratio (OMLR) in figure 14(b) and (c). We utilized the observed redshift to estimated the 3-dimensional distribution of the galaxy, assuming the spherical symmetry. The IMLR and OMLR are calculated to be  $\sim 4.0 \times 10^{-3} M_\odot/L_\odot$  and  $4.3 \times 10^{-2} M_\odot/L_\odot$  within  $r \lesssim 380$  kpc. Both are subjected to large errors, and we tentatively adopted factors of two and three, respectively, in figure 14.

We summarize recent measurements of IMLR and OMLR in table 10. NGC 720 and the Centaurus cluster exhibit similar values with A 1060 when compared at the same radius, while the Fornax cluster shows significantly smaller values by an order of magnitude. It is suggested that the smaller systems with lower gas temperature tend to show lower IMLR in Makishima et al. (2001), however its deviation is outstanding.

Both the integrated IMLR and OMLR steeply increase up to  $\sim 100$  kpc and seem to reach almost maximum at 100–200 kpc. This trend is similar to the IMLR obtained with XMM-Newton for M 87 and the Centaurus cluster by Matsushita et al. (2007b) within  $r \lesssim 100$  kpc. The steep increase in the  $r \lesssim 100$  kpc region suggests that the Fe and O ions which was synthesized in the central galaxies have diffused to the ICM. On the other hand, as pointed out in Ezawa et al. (1997), abundance gradient over a few hundred kpc scale in clusters of galaxies should follow the mass ratio between the galaxies and the ICM gas. This is because heavy ions released from galaxies without much kinetic energy would not diffuse out more than 10 kpc over the Hubble time. (Böhringer et al. 2004) indicated that it takes about  $10^{10}$  yr to synthesize Fe mass within  $r \lesssim 100$  kpc range.

These considerations suggest that both Fe and O enriched gas was released to the ICM space with significant kinetic energy and/or the gas stripping was efficiently occurred in the  $\sim 100$  kpc range due to the galactic motion. We also note that two central galaxies (NGC 3311 and NGC 3309) of A 1060 are slightly off-center ( $\sim 0.3'$  and  $2'$ ) from the X-ray peak of the cluster (see figure 1(b) of Hayakawa et al. 2006), and the line of sight velocity is calculated to be  $180 \text{ km s}^{-1}$  and  $660 \text{ km s}^{-1}$ . Ram-pressure

stripping is also likely to be the reason why these central galaxies show very compact X-ray halo (Yamasaki et al. 2002).

The obtained O mass in figure 14(a) provides the rough estimate of the SN II rate. Theoretical calculations (Nomoto et al. 2006; Thielemann et al. 1996; Tsujimoto et al. 1995) predict the O product of  $\sim 1.5 M_{\odot}$  for  $20 M_{\odot}$  progenitor mass and  $\sim 9 M_{\odot}$  for  $40 M_{\odot}$  progenitor. This requires at least  $\sim 3 \times 10^9$  SN II in the whole cluster since the formation.

#### 5.4. Warm Component in the Galactic Emission

As shown in figure 11(a), the association of O VIII line and the ICM is evident. The surface brightness of O VII lines are brighter than the level of NGC 2992 region or than the average of wider sky region (McCammon et al. 2002), but consistent with the uniform distribution over the cluster. A large fraction of O VII photons is considered to be originated from the Milky Way Halo, whose typical temperature measured with XMM-Newton is  $kT \sim 0.2$  keV (Lumb et al. 2002). If there is a cooler component like Local Hot Bubble,  $kT \sim 0.08$  keV by Lumb et al. (2002); Snowden et al. (1998), or Warm-Hot Intergalactic Medium, it is hard to detect it under the strong emission from the ICM. Our spectral fit showed that a  $kT \sim 0.7$  keV component was required to reproduce the spectral structure around the Fe L-line complex. The surface brightness of this component shows a flat distribution in our field of view (subsection 4.3). The ROSAT 3/4 keV image shows an enhancement with an angular extent of  $\sim 10 \times 20$  deg<sup>2</sup>, which may be an extension of the North Polar Spur (Snowden et al. 1997). These features suggest that the  $\sim 0.7$  keV component is a Galactic origin, but a further study is certainly needed and it is beyond the scope of this paper.

Authors are grateful to K. Dolag for supplying the simulation data and S. Sasaki for discussions. We also thank the referee for providing valuable comments. Part of this work was financially supported by the Ministry of Education, Culture, Sports, Science and Technology of Japan, Grant-in-Aid for Scientific Research No. 14079103, 15340088, 15001002.

#### Appendix 1. Fraction from Corresponding Sky

Since angular resolution of X-Ray Telescopes (XRT; Serlemitsos et al. 2007) of Suzaku ( $\sim 2'$  in half power diameter; HPD) is not as good as those of Chandra ( $\sim 0.5''$ ) and XMM-Newton ( $\sim 15''$ ), fraction of photons may become significant that come from outside of the sky direction corresponding to the extraction region of spectra on the XIS detector plane. This was a severe problem for the ASCA GIS (Ohashi et al. 1996; Makishima et al. 1996), which employs similar type of thin-foil-nested reflectors for the XRT (Serlemitsos et al. 1995) with  $\sim 3.6'$  HPD, and the fraction sometimes became more than half of total detected photons as seen in figure 4 of Kikuchi et al. (1999) for the MKW 3s and 2A 0335+096 clusters. It

made the cluster analysis further complicated that energy dependence of the fraction could not be neglected with the ASCA XRT/GIS system.

The situation has been much improved for Suzaku than ASCA. The Suzaku XRT/XIS system adopts longer focal length of 4.75 m than ASCA (3.5 m) and the sky coverage of the XIS detector ( $18' \times 18'$ ) is smaller than the GIS ( $\sim 22'$  radius), so that the energy-dependent vignetting effect is much smaller. Moreover, improvement of the mirror surface has reduced scatters on the reflector and equipment of the pre-collimator dramatically decreased the so-called “stray-lights” mainly from outside of the XIS field of view (Serlemitsos et al. 2007).<sup>3</sup>

We therefore estimated the fraction of photons outside the extraction region using a simulator of the Suzaku XRT/XIS system, “xissim” version 2006-08-26 (Ishisaki et al. 2007), in the following way: (1) Assuming the double- $\beta$  model surface brightness profile (table 3), 2,000,000 count of monochromatic incident-photons (in 0.5, 1, 2, 4, or 8 keV) were generated by a “mkphlist” task. (2) Simulated event files were created for both the central and offset observations using the “xissim” task, with the `xis_efficiency` parameter set to “no” to save photon statistics. (3) Using the RA and DEC columns in the simulated event files, the event files were splitted into 7+1 sky regions corresponding to the extraction annuli of 0–2', 2–4', 4–6', 6–9', 9–13', 13–17', and 17–27', plus outside of them,  $r > 27'$ .<sup>4</sup> (4) The detected photon count at each extraction region on the XIS detector plane was calculated for each splitted event file using the “xselect” task.

In this way, we estimated the fraction of photons for the 7 extraction annuli from the 8 sky regions in 5 energies for the 4 XIS sensors. We plot examples of BI (XIS1) in figure 15. It is confirmed that more than 65% of photons are coming from the corresponding sky directions by the “xissim” simulations. The energy dependence is almost negligible within  $\sim 5\%$  in figure 15(h). Fractions from the second next to the noticed annulus are less than  $\sim 1\%$  at the offset observation, even though the surface brightness of the central part of the cluster is much brighter by orders of magnitude (figure 4). This is primarily owing to the existence of the pre-collimator for the Suzaku XRT. These results are almost the same with the other XIS sensors. Note that this simulation does not include the CXB and the Galactic background, which are almost uniform on the sky so that the spatial response is different from figure 15.

#### Appendix 2. Dependence on Abundance Tables

There are several abundance tables usable in XSPEC, such as *angr* (Anders & Grevesse 1989), *aneb* (Anders & Ebihara 1982), *feld* (Feldman 1992), and *lodd* (Lodders 2003). The elemental abundances relative to hydrogen in

<sup>3</sup> The “stray-lights” reach to the focal plain through abnormal paths, e.g., reflection by only the secondary mirror, or the mirror backside reflection (Mori et al. 2005).

<sup>4</sup> The “fselect” task with the *angsep* function was utilized to calculate the angular separation of events from the assumed center of the cluster, (RA, Dec) = ( $10^{\text{h}}36^{\text{m}}42^{\text{s}}.8$ ,  $-27^{\circ}31'42''$ ).

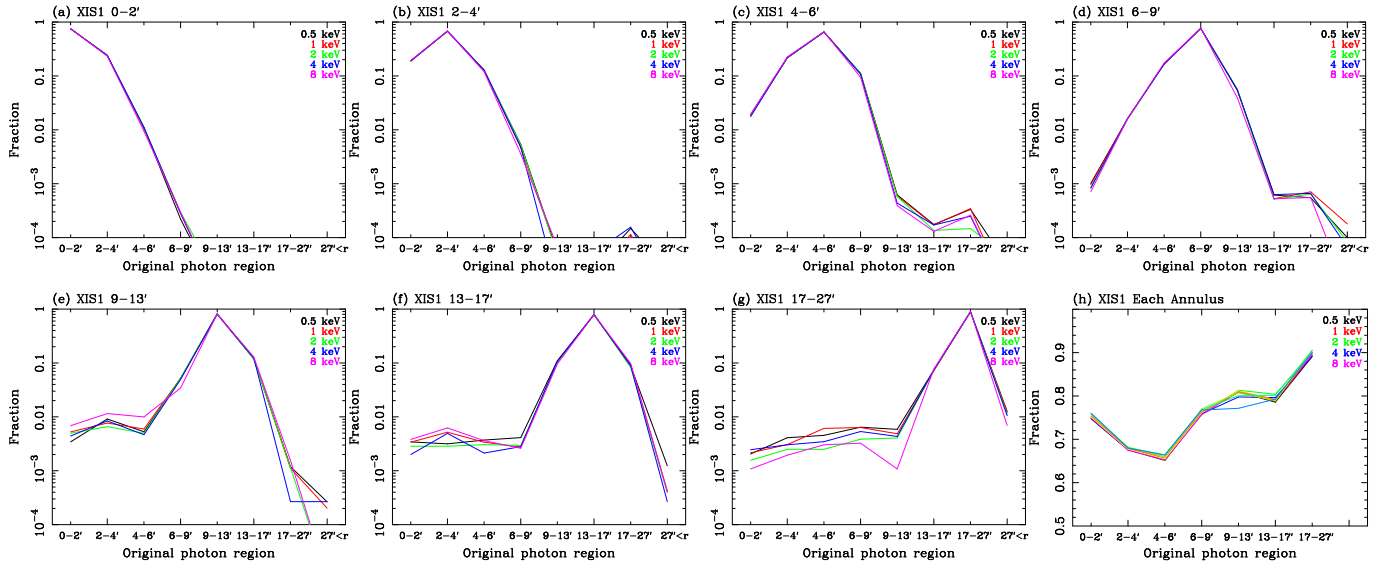


**Fig. 15.** (a)–(g) Fraction of photons detected in the 0–2′ to 17–27′ extraction regions on the BI (XIS1) sensor plotted against the original sky directions of incidence, which is estimated by the “xissim” simulation. Different energies are plotted in different colors. (h) Photon fraction of each annulus coming from the corresponding sky region, i.e., maximum values of panels (a)–(g) are plotted.

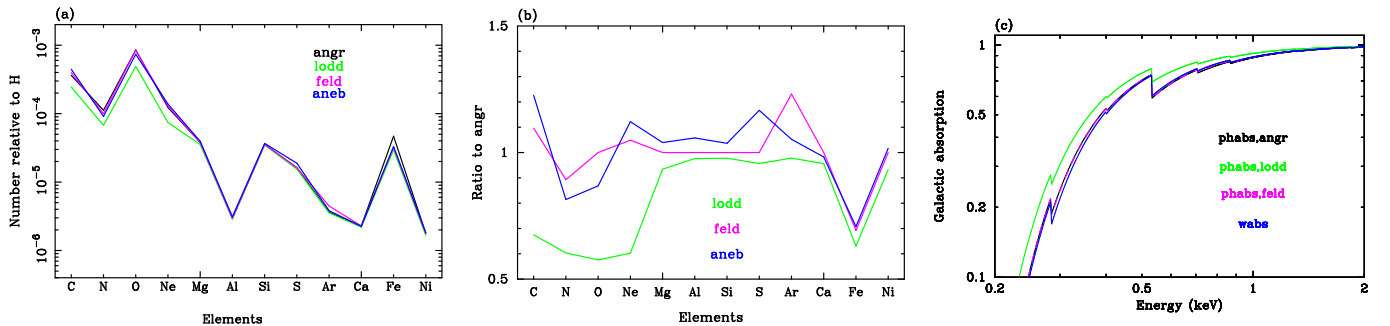


**Fig. 16.** (a) The assumed metal abundances relative to H in number by the *angr*, *lodd*, *feld*, and *aneb* tables of XSPEC v11.3.0t. (b) Same as (a) but normalized by the *angr* abundances. (c) Comparison of absorption by the *phabs* model with *angr* abundance table, *phabs* with *lodd*, and the *wabs* model in XSPEC. The *wabs* model assumes the abundance ratio of *aneb* built-in the code. Neutral hydrogen column density of  $N_{\text{H}} = 4.9 \times 10^{20} \text{ cm}^{-2}$  and “1 solar” abundance, which is different among the tables, are assumed. The photoelectric absorption cross-section of *bcmc* (Bałucińska-Church & McCammon 1992; Yan et al. 1998) is used.

number defined by these tables are plotted in figure 16(a), and ratios of each element to *angr* is shown in figure 16(b). Although *feld* is not used in our spectral analysis, it is added to compare recent Suzaku results (Matsushita et al. 2007a; Tawara et al. 2007) which adopt this table. As seen in figure 16(b), *angr* and *feld* are essentially the same except for Fe abundance, which is 1.44 times larger for *angr* than *feld*.

The *angr* table is the de facto of XSPEC, however, Fe abundance is significantly different from others. This is because *angr* is based on the solar photospheric measurement of Fe I (Blackwell et al. 1984), which disagrees with the meteorites measurement adopted in *aneb*. Discussions afterwards seem to prefer the lower abundance by meteorites, because Fe abundance determined by Fe II, which is dominant in the solar photosphere, is consistent with the meteorites value (Biemont et al. 1991; Raassen & Uylings 1998).

It is notable that C, N, O, and Ne abundances in *lodd*

is significantly lower ( $\sim 60\%$  of *angr*). These values are based on the three-dimensional time-dependent hydrodynamical model solar atmosphere, in which departures from local thermodynamical equilibrium (LTE) and blend of Ni I line with the forbidden [O I]  $\lambda 6300$  are considered (Allende Prieto et al. 2001; Allende Prieto et al. 2002). The *lodd* table in XSPEC is the recommended elemental abundance of the solar photosphere (table 1 in Lodders 2003), however, he states that the photo-solar abundances as representative of the solar system should be slightly larger (by  $\sim 1.2$  times for C, N, and O) for helium and heavy-element due to the settling effects.

The decrease of these abundant elements in the Inter Stellar Medium (ISM) also leads to the difference in the assumed Galactic absorption as seen in figure 16(c). The *phabs* absorption model with *lodd* abundance table gives by  $\sim 15\%$  smaller absorption at the maximum in our noticed energy range of 0.4–7.1 keV in the spectral fitting, while the difference between *wabs* and *phabs* with *angr* is

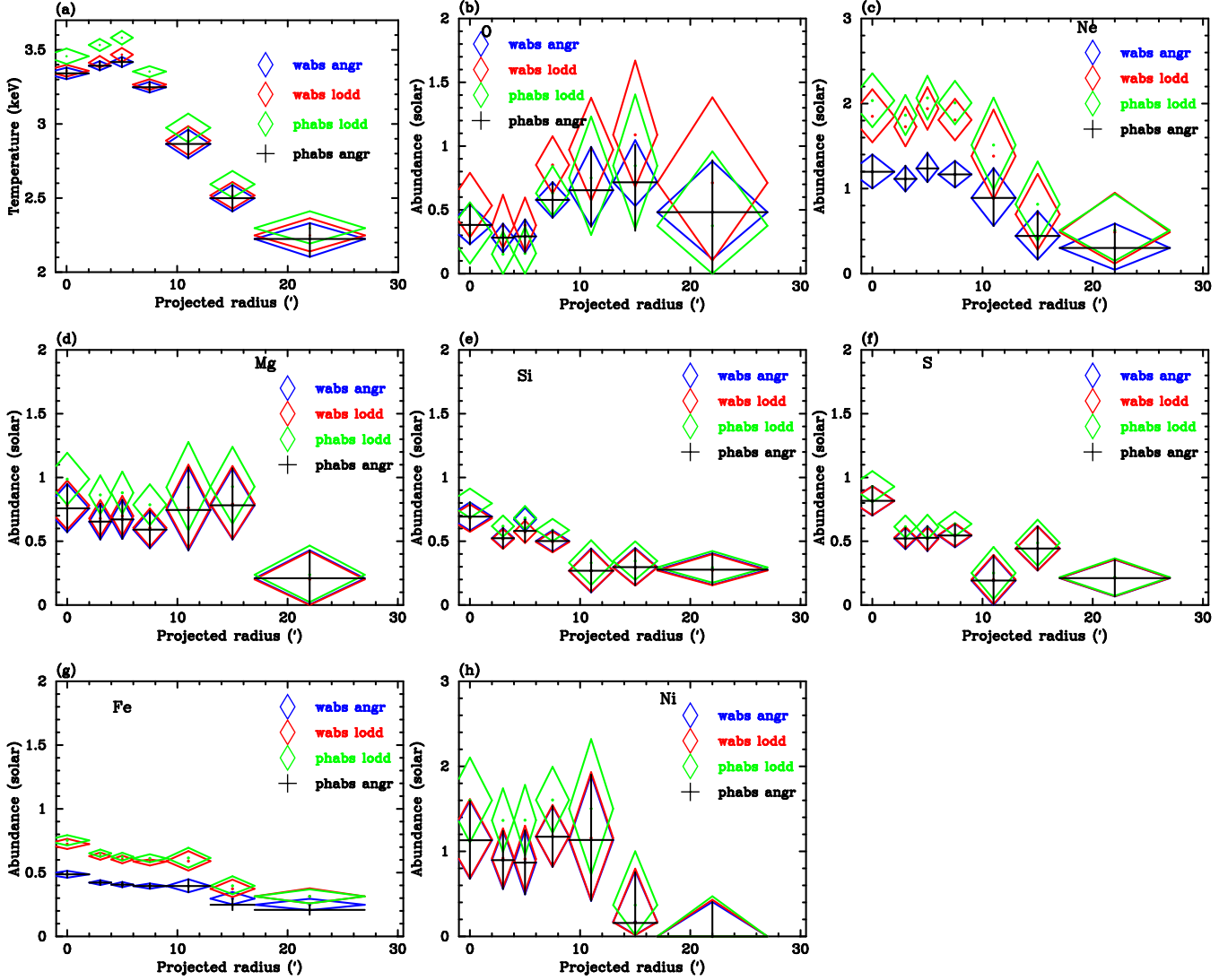


Fig. 17. Same as figure 10 of the Suzaku result for the black crosses (*phabs angr*). Other fit results are also plotted in blue, red, and green diamonds, when different abundance ratio (*lodd*) and/or different absorption model (*wabs*) are assumed.

Table 11. List of  $\chi^2/\text{dof}$  for each fit.

Region	O, Ne, Mg independent				Constrained to be O=Ne=Mg			
	<i>phabs angr</i>	<i>wabs angr</i>	<i>wabs lodd</i>	<i>phabs lodd</i>	<i>phabs angr</i>	<i>wabs angr</i>	<i>wabs lodd</i>	<i>phabs lodd</i>
0–2'	1240/992	1240/992	1215/992	1274/992	1278/996	1260/996	1258/996	1335/996
2–4'	1290/992	1290/992	1267/992	1356/992	1358/996	1346/996	1343/996	1464/996
4–6'	1345/992	1345/992	1312/992	1400/992	1418/996	1396/996	1397/996	1513/996
6–9'	1329/992	1329/992	1298/992	1395/992	1365/996	1340/996	1359/996	1464/996
9–13'	1057/992	1057/992	1053/992	1059/992	1058/996	1057/996	1057/996	1063/996
13–17'	1082/992	1082/992	1077/992	1078/992	1086/996	1085/996	1080/996	1080/996

negligible. This is because we have assumed the neutral hydrogen column density of  $N_{\text{H}} = 4.9 \times 10^{20} \text{ cm}^{-2}$  (Dickey & Lockman 1990) with “1 solar” abundance for the ISM. In fact, the ISM consists of monoatomic gas, molecules, and grains, so that it is suggested to have smaller abundance than the solar abundance by Wilms et al. (2000). Shaver et al. (1983) have reported a radial abundance gra-

dent in the Milky Way Galaxy of  $\sim 16\%$  per kpc.

Considering these uncertainties, we have tested the spectral fit of A 1060 with four kinds of combinations in the absorption model and the abundance table, *phabs angr*, *wabs angr*, *wabs lodd*, and *phabs lodd*. We further tested the fit when the abundances of O, Ne, and Mg are linked to have the same value relative to the assumed “so-

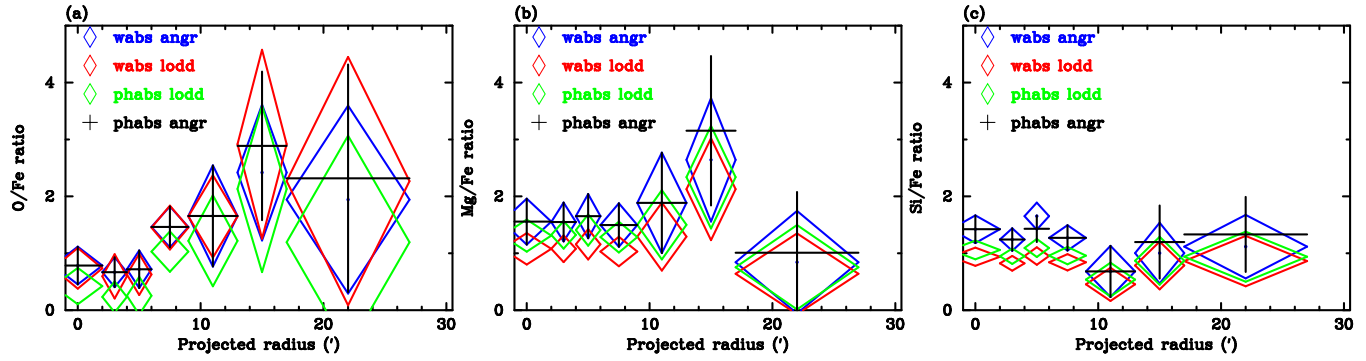


Fig. 18. (a) O/Fe ratio, (b) Mg/Fe ratio, and (c) Si/Fe ratio, which are same as figure 13(a) for the black crosses (*phabs angr*) in these figures (a)–(c). Other fit results are also plotted in blue, red, and green diamonds, when different abundance ratio (*lodd*) and/or different absorption model (*wabs*) are assumed.

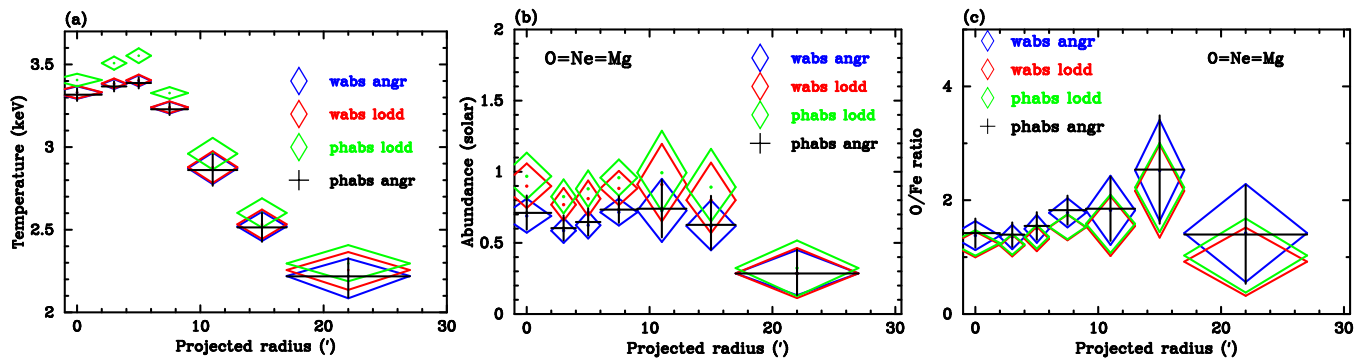


Fig. 19. Radial profiles of (a) temperature, (b)  $O = Ne = Mg$  abundance, and (c) abundance ratio to Fe, when the abundances of O, Ne, and Mg are constrained to have the same value for the assumed abundance tables of *anгр* or *lodd*. Meaning of the markers are same as figures 17 and 18.

lar” abundance, in two reasons: they are all supposed to be primarily the SN II products; O and Ne abundances are susceptible to the Galactic component in outer annuli. Note that the O : Ne : Mg ratios are significantly different between *anгр* (1 : 0.145 : 0.045) and *lodd* (1 : 0.151 : 0.072).

Results are summarized in figures 17–19 and a list of  $\chi^2/\text{dof}$  is presented in table 11. As expected from figure 16(c), the *phabs anгр* and *wabs anгр* results are almost identical. The *phabs lodd* gives slightly larger temperature than others, which leads the O abundance profile in figure 17(b) to be different behavior from others. Other discrepancies in the derived abundances can be explained by difference in the definition of “1 solar”.

Since  $\chi^2$  values for *phabs lodd* are generally larger than other models, the Galactic absorption model by *phabs lodd* is considered to be inappropriate with our X-ray data. On the other hand, *wabs lodd* model shows the minimum  $\chi^2$  in table 11. This is interesting because the *wabs* absorption model assumes *aneb* abundance table built-in the code. This may indicates that our modeling of the Galactic component is too naive, and/or the Galactic abundance gradient is responsible so that effective elemental abundance between absorption and emission are different.

It is notable that shape of the radial abundance profiles are quite similar among these four models in figure 19 when  $O = Ne = Mg$  is assumed. Difference from Fe or Si

is evident as seen in figures 18(c) and 19(c): Fe and Si abundances decreases with radius with roughly constant Si/Fe ratio, while  $O = Ne = Mg$  are almost constant within  $r \lesssim 17'$ . The higher  $(O = Ne = Mg)/Fe$  ratio than “1 solar” is also suggested for both *anгр* and *lodd* abundance tables.

## References

- Allende Prieto, C., Lambert, D. L., & Asplund, M. 2001, ApJL, 556, L63
- Allende Prieto, C., Lambert, D. L., & Asplund, M. 2002, ApJL, 573, L137
- Anders, E., & Ebihara, M. 1982, Geochim. Cosmochim. Acta, 46, 2363
- Anders, E., & Grevesse, N. 1989, Geochim. Cosmochim. Acta, 53, 197
- Arnaud, M., Rothenflug, R., Boulade, O., Vigroux, L., & Vangioni-Flam, E. 1992, A&A, 254, 49
- Balucińska-Church, M., & McCammon, D. 1992, ApJ, 400, 699
- Biemont, E., Baudoux, M., Kurucz, R. L., Ansbacher, W., & Pinnington, E. H. 1991, A&A, 249, 539
- Blackwell, D. E., Booth, A. J., & Petford, A. D. 1984, A&A, 132, 236
- Böhringer, H., Matsushita, K., Churazov, E., Finoguenov, A., & Ikebe, Y. 2004, A&A, 416, L21
- Brandt, W. N., & Hasinger, G. 2005, ARA&A, 43, 827
- Christlein, D., & Zabludoff, A. I., 2003, ApJ, 591, 764

- Ciotti, L., Pellegrini, S., Renzini, A., & D'Ercole, A. 1991, *ApJ*, 376, 380
- De Grandi, S., & Molendi, S., 2001 *ApJ*, 551, 153
- De Grandi, S., Ettori, S., Longhetti, M., & Molendi, S. 2004, *A&A*, 419, 7
- Dickey, J. M., & Lockman, F. J. 1990, *ARA&A*, 28, 215
- Dolag, K., Grasso, D., Springel, V., & Tkachev, I. 2004, *Journal of Experimental and Theoretical Physics Letters*, 79, 583
- Dolag, K., Hansen, F. K., Roncarelli, M., & Moscardini, L. 2005, *MNRAS*, 363, 29
- Ezawa, H. et al. 1997, *ApJL*, 490, 33
- Feldman, U. 1992, *Phys. Scr.*, 46, 202
- Finoguenov, A., David, L. P., & Ponman, T. J. 2000, *ApJ*, 544, 188
- Finoguenov, A., Arnaud, M., & David, L. P. 2001, *ApJ*, 555, 191
- Finoguenov, A., Matsushita, K., Böhringer, H., Ikebe, Y., & Arnaud, M. 2002, *A&A*, 381, 21
- Fujimoto, R. et al. 2007, *PASJ*, in press
- Fukazawa, Y., Makishima, K., Tamura, T., Ezawa, H., Xu, H., Ikebe, Y., Kikuchi, K., & Ohashi, T. 1998, *PASJ*, 50, 187
- Fukazawa, Y., Makishima, K., Tamura, T., Nakazawa, K., Ezawa, H., Ikebe, Y., Kikuchi, K., & Ohashi, T. 2000, *MNRAS*, 313, 21
- Fukazawa, Y., Kawano, N., & Kawashima, K. 2004, *ApJL*, 606, L109
- Furusho, T., Yamasaki, N. Y., Ohashi, T. S. R., Kagei, T., Ishisaki, Y., Kikuchi, K., Ezawa, H., & Ikebe, Y. 2001, *PASJ*, 53, 421
- Hayakawa, A., Furusho, T., Yamasaki, N. Y., Ishida, M., & Ohashi, T. 2004, *PASJ*, 56, 743
- Hayakawa, A., Hoshino, A., Ishida, M., Furusho, T., Yamasaki, N. Y., & Ohashi, T. 2006, *PASJ*, 58, 743
- Ishisaki, Y., et al. 2007, *PASJ*, in press
- Kikuchi, K., Furusho, T., Ezawa, H., Yamasaki, N. Y., Ohashi, T., Fukazawa, Y., & Ikebe, Y. 1999, *PASJ*, 51, 301
- Koyama, K. et al. 2006, *PASJ*, in press
- Kushino, A., Ishisaki, Y., Morita, U., Yamasaki, N. Y., Ishida, M., Ohashi, T., & Ueda, Y. 2002, *PASJ*, 54, 327
- Kawahara, H., et al. 2007, *ApJ*, in press [astro-ph/0611018]
- Loewenstein, M. 2001, *ApJ*, 557, 573
- Lodders, K. 2003, *ApJ*, 591, 1220
- Lumb, D. H., Warwick, R. S., Page, M., & De Luca, A. 2002, *A&A*, 389, 93
- Makishima, K., et al. 1996, *PASJ*, 48, 171
- Makishima, K., et al. 2001, *PASJ*, 53, 401
- Markevitch, M., et al. 1998, *ApJ*, 503, 77
- Matsushita, K., Finoguenov, A., Böhringer, H. 2003, *A&A*, 401, 443
- Matsushita, K., et al. 2007 *PASJ*, in press [astro-ph/0609065]
- Matsushita, K., et al. 2007 *A&A*, in press [astro-ph/0610293]
- Matteucci, F., Panagia, N., Pipino, A., Mannucci, F., Recchi, S., & Della Valle, M. 2006, *MNRAS*, 372, 265
- Mazzotta, P., Rasia, E., Moscardini, L., & Tormen, G. 2004, *MNRAS*, 354, 10
- McCammon, D., et al. 2002, *ApJ*, 576, 188
- Mewe, R., Gronenschild, E. H. B. M., & van den Oord, G. H. J. 1985, *A&AS*, 62, 197
- Mewe, R., Lemen, J. R., & van den Oord, G. H. J. 1986, *A&AS*, 65, 511
- Mitsuda, K. et al. 2007, *PASJ*, in press
- Mori, H., et al. 2005, *PASJ*, 57, 245
- Morrison, R., & McCammon, D. 1983, *ApJ*, 270, 119
- Nomoto, K., Tominaga, N., Umeda, H., Kobayashi, C., & Maeda, K. 2006, [astro-ph/0605725]
- Ohashi, T., et al. 1996, *PASJ*, 48, 157
- Raassen, A. J. J., & Uylings, P. H. M. 1998, *A&A*, 340, 300
- Renzini, A., Ciotti, L., D'Ercole, A., & Pellegrini, S. 1993, *ApJ*, 419, 52
- Renzini, A. 1997, *ApJ*, 488, 35
- Sato, K., Furusho, T., Yamasaki, N. Y., Ishida, M., Matsushita, K., & Ohashi, T. 2005, *PASJ*, 57, 743
- Serlemitsos, P. J., et al. 1995, *PASJ*, 47, 105
- Serlemitsos, P. J., et al. 2007, *PASJ*, in press
- Shaver, P. A., McGee, R. X., Newton, L. M., Danks, A. C., & Pottasch, S. R. 1983, *MNRAS*, 204, 53
- Smith, R. K., Brickhouse, N. S., Liedahl, D. A., & Raymond, J. C. 2001, *ApJL*, 556, L91
- Snowden, S. L., Egger, R., Freyberg, M. J., McCammon, D., Plucinsky, P. P., Sanders, W. T., Schmitt, J. H. M. M., Truemper, J. and Voges, W. 1998, *ApJ*, 493, 715
- Snowden, S. L., Egger, R., Finkbeiner, D. P., Freyberg, M. J., & Plucinsky, P. P. 1998, *ApJ*, 493, 715
- Strickland, D.K., & Stevens, I.R., 2000, *MNRAS*, 314,511
- Tamura, T., et al. 1996, *PASJ*, 48, 671
- Tamura, T., Kaastra, J. S., Makishima, K., & Takahashi, I. 2003, *A&A*, 399, 497
- Tamura, T., Kaastra, J. S., den Herder, J. W. A., Bleeker, J. A. M., & Peterson, J. R. 2004, *A&A*, 420, 135
- Tawara, Y., et al. 2007, *PASJ*, submitted
- Thielemann, F.-K., Nomoto, K., & Hashimoto, M. 1996, *ApJ*, 460, 408
- Tsujimoto, T., Nomoto, K., Yoshii, Y., Hashimoto, M., Yanagida, S., & Thielemann, F.-K. 1995, *MNRAS*, 277, 945
- Vikhlinin, A., Markevitch, M., Murray, S. S., Jones, C., Forman, W., & Van Speybroeck, L. 2005, *ApJ*, 628, 655
- Wilms, J., Allen, A., & McCray, R. 2000, *ApJ*, 542, 914
- Yamasaki, N. Y., Ohashi, T., & Furusho, T. 2002, *ApJ*, 578, 833
- Yan, M., Sadeghpour, H. R., & Dalgarno, A. 1998, *ApJ*, 496, 1044
- Yoshida, N., Bromm, V., & Hernquist, L. 2004, *ApJ*, 605, 579
- Yoshikawa, K., Yamasaki, N. Y., Suto, Y., Ohashi, T., Mitsuda, K., Tawara, Y., & Furuzawa, A. 2003, *PASJ*, 55, 879
- Yoshikawa, K., et al. 2004, *PASJ*, 56, 939